Electronic Supplementary Material (ESI) for Energy & Environmental Science.

Supporting Information

Hydrogen Generation via Ammonia Decomposition on Highly Efficient and Stable Ru-free Catalysts: Approaching Complete Conversion at 450 ^oC

Hassina Tabassum,+,1 Shreya Mukherjee,+,1 Junjie Chen,+,1 Domoina Holiharimanana,+,2 Stavros Karakalos,[3] Xiaoxuan Yang,[1] Sooyeon Hwang,[4,*] Tianyu Zhang,[2] Bo Lu,[5] Min Chen,[5] Zhong Tang,[5] Eleni A. Kyriakidou,[1,*] Qingfeng Ge,[2,*] and Gang Wu[1,*]

[1]Department of Chemical and Biological Engineering, University at Buffalo, The State University of New York, Buffalo, New York 14530, USA. Email: gangwu@buffalo.edu (G.Wu) and elenikyr@buffalo.edu (E.A. Kyriakidou)

[2]Department of Chemistry and Biochemistry, Southern Illinois University, Carbondale, Illinois 62901, USA. Email: qge@chem.siu.edu (Q. Ge)

[3]Department of Chemical Engineering, University of South Carolina, Columbia, South Carolina 29208, USA

[4]Center for Functional Nanomaterials, Brookhaven National Laboratory, Upton, New York 11973, USA. Email: soohwang@bnl.gov (S. Hwang)

[5]Bettergy Corp., Peekskill, New York 10566, USA

+These authors contributed equally

*Corresponding authors

Experimental Details
Figures S1-S31
Tables S1 to S10

Experimental details

Catalyst synthesis.

Chemicals used are cobalt nitrate (II) hexahydrate, 99% pure (ACROS Organics), nickel nitrate (II) hexahydrate, 99% pure (ACROS Organics), magnesium nitrate hexahydrate, 99% pure (ACROS Organics), strontium nitrate anhydrous, 99.97% pure (Alfa Aesar), cerium nitrate (III) hexahydrate (>99%), potassium nitrate (Alfa Aesar), potassium hydroxide (KOH) pellets (Alfa Aesar). Catalysts were synthesized by using co-precipitation methods. KOH was used as the precipitating agent, and its concentration (1M, 2M, 3M, 4M, and 5M) has been optimized to increase nucleation and reduce the crystallite size. Typically, metal nitrates of Mg, Sr, Ce were taken in a molar ratio of 2:1:1 and mixed in 125 ml water for the optimal catalyst. Meanwhile, cobalt and nickel salts were taken in a molar ratio of 2:1 in the same volume of water with a total metal loading of 60 wt.% of total metals in the solution. A separate solution of concentrated KOH (4.0 M for K-Promoted catalyst) was prepared. The metal nitrate solution was added to the KOH solution dropwise while stirring vigorously. After complete mixing, the stirring was stopped, and the solution was aged for 22 hours at room temperature. After 22 h, the precipitate was separated by centrifugation and washed with water four times, followed by drying at 60 °C for 12 h. After drying, the residue was collected and ground in mortar and pestle before thermal treatment. The powder sample containing mixed hydroxides and oxides was then thermally reduced under 10% H_2 balanced by Ar at 600 °C for one hour at a ramping rate of 2 °C min^{-1}. Initially, mixed oxides of Co, Ni, Mg, Ce, and Sr were produced. During the holding temperature at 600 °C, Co and Ni species were completely reduced, forming CoNi alloys, while Mg, Ce, and Sr remained as a mixed oxide. The resulting catalyst was denoted as the K- $CoNi_{alloy}$-MgO-CeO_2-SrO.

Catalyst performance evaluation

The prescreening of all the catalysts was done in a fixed bed reactor of 4 mm ID and 6 mm OD with a bed length of 1.0 cm, including quartz wool. The quartz wool was used to prevent the flushing out of the catalyst powders during testing, as shown in **Figure S10**. Ar was used as a sweep gas during the thermal activation at 600 °C for one hour. The feed gas was changed to 99.9999% pure NH_3 at the target temperature. An acid trap was used at the outlet to collect the unconverted NH_3. The mass flow controller was used at the inlet to control the inlet gas flow rate, while a calibrated mass flow meter was used at the outlet to measure nitrogen and hydrogen flow rates. The H_2 and N_2 ratio were confirmed using a gas chromatograph (GC, Agilent). A blank test was conducted to indicate that the conversion of NH_3 is less than 1% at 575 °C. The stability of the optimized catalyst was tested in an industrial membrane reactor shown in **Figure S15**. The variation in activity with pressure was also monitored in the fixed bed reactor and the membrane reactor.

100 mg catalyst was loaded into the reactor for finding the GHSV in mL g_{cat}^{-1} h^{-1}. 300 mg catalyst was loaded in the reactor for each test to cover 0.5 cm of the bed. Gas hour space velocity was calculated as the ratio of the volume of feed gas in mL/h and the volume of the bed (mL), GHSV =h^{-1}. The catalyst was plugged using quartz wool to prevent displacement and loss of catalyst bed. The feed gas flow rate was varied between 10 to 120 sccm to monitor activity at different space velocities. An acid trap was used at the outlet to collect the unconverted NH_3. The mass flow controller was used at the inlet to control the inlet gas flow rate, while a calibrated mass flow meter was used at the outlet to measure the flow rates of N_2 and H_2. The H_2 and N_2 ratio was confirmed using a GC. The NH_3 conversions (X_{NH3}), H_2 production rates, and TOF were calculated (**Eqs. 1-3**).

$$X_{NH3} = (F_{gas\ outlet} - F_{gas\ inlet})/ F_{gas\ inlet} \times 100\% \qquad \text{(Eq. 1)}$$

Where $F_{gas\ outlet}$ and $F_{gas\ inlet}$ represent molar flow rate of inlet and outlet gas, respectively.

$$H_2 \text{ production rate} = ((3/2) \times F_{gas\ inlet} \times X_{NH3})/\text{Catalyst loading} \qquad \text{(Eq. 2)}$$

$$\text{TOF} = H_2 \text{ production rate } (\text{mmol } g_{CoNi}^{-1} \text{ min}^{-1})/\text{Active site density} \qquad \text{(Eq. 3)}$$

Active site density was determined by the CO pulse chemisorption.

Catalyst Characterization

The X-ray diffraction (XRD) patterns of the samples were recorded on the Rigaku Ultima IV diffractometer with Cu Kα X-rays operating at 200 mA and 40 kV, using Cu *Kα* as the radiation source (λ = 0.15418 nm). A Thermo-Fisher Talos F200X transmission electron microscope with a Super-X energy disperse spectroscopy (EDS) system was used for electron microscopy studies. Powder samples were deposited on a standard microscope glass slide. In-situ X-ray photoelectron spectroscopy (XPS) was conducted using a Kratos AXIS Ultra DLD XPS system equipped with a hemispherical energy analyzer and a monochromatic Al Kα source operated at 15 keV and 150 W; the pass energy was fixed at 40 eV for the high-resolution scans. The curve fitting procedure was carried out using the XPS Peak 41 software. The peak approximation was carried out by a combination of Gaussian - Lorentzian functions, with subtraction of Shirley-type background. The in-situ treatment of the catalyst at various temperatures and atmospheres was performed in a reaction cell (Model: ES-009R01) directly attached to the XPS chamber, which allows the sample to be treated at gas flow conditions. The samples were transferred inside the reaction cell and back to the analysis chamber without exposure to the atmosphere. Before analysis, the samples were placed in a vacuum at 80 °C overnight to remove the adsorbed substances. The specific surface area (S_{BET}) measurements were carried out using N_2 adsorption/desorption at 77 K on a Micromeritics TriStar II instrument. Samples were degassed at 130 °C for five hours under vacuum before nitrogen physisorption measurements. The S_{BET} was determined from the linear part of the BET curve.

H_2 temperature-programmed reduction (H_2-TPR) and CO pulse chemisorption experiments were conducted on a Micromeritic AutoChem II 2920 instrument with a thermal conductivity detector (TCD). About 50 mg of each sample was used in all those tests. For the H_2-TPR test, the catalysts were first pre-treated under 20% O_2/Ar (Air gas) at 400 ^oC for one hour. Then, the catalysts were cooled down to ambient temperature and purged with Ar (ultra-high purity, Air gas) for 30 min to remove gas-phase O_2, and 50 sccm (cm^3/min, STP) of 10% H_2/Ar (Air gas) was introduced to the reactor. After the TCD signal stabilized, the catalyst was heated up to 800 ^oC (10 ^oC /min) under 10% H_2/Ar. The mobility and redox properties of catalyst samples were evaluated via H_2-TPR measurement using H_2 as a reductant. TCD recorded the H_2 consumption profiles as a function of temperature. The same reduction pre-treatment (10% H_2/Ar, 600 ^oC, 60 min) was applied for the CO pulse chemisorption. After completing the pre-treatment step, the catalysts were purged with 100% He (Praxair) for another 30 min at 600 ^oC following by cooling down to 35 ^oC before the CO pulse chemisorption experiments. A series of 10% CO/He (Air-gas) pulses were injected in the reactor until the catalyst surface was saturated by CO. A stoichiometry ratio of chemisorbed CO to surface-active metal atom = 1:1 was applied to calculate the number of active sites. The TOF of NH_3 on the catalysts can be calculated from the amount of converted NH_3 molecules per exposed surface, calculated from CO pulse chemisorption.[1]

CO_2 temperature-programmed desorption (CO_2-TPD) was performed in a custom-build micro-reactor system, as reported previously.[2-4] A mass spectrometer (Pfeiffer Omnistar GSD 320) is connected to the outlet of the reactor as a detector. 50 mg of catalyst was loaded in a U-shape reactor (I.D. = 8 mm). The catalyst was first pre-treated with 10% H_2/Ar at 600 °C for one hour, then purged with pure Ar for 30 min to remove H_2. The catalyst was then cooled down to room temperature and exposed to 80% CO_2/Ar for one h. The catalyst surface was saturated with CO_2, following by purging with Ar for another 30 min to remove gas-phase CO_2. Finally, the catalyst was heated up to 800 °C (10 °C/min). A mass spectrometer recorded the CO_2 (m/z = 44) desorption profiles. Quantities desorbed at a specific temperature give information about the number, strength, and heterogeneity of adsorption sites.

NH_3 TPD experiments: 300 mg of catalyst was used for the NH_3 temperature-programmed decomposition experiments. The catalysts were pre-treated with 10% H_2/Ar at 600 °C for one hour, then cooled down to 200 °C under the same feed gas. The catalyst was then purged with pure Ar for 30 min to remove H_2 from the catalyst surface and cooled down to 100 °C before 100 sccm 10% NH_3/Ar was introduced to the reactor. The gas concentrations were stabilized, followed by the heating up of the catalyst to 575 °C (2.5 °C/min). The temperature was kept at 575 °C for 30 min, followed by cooling down to 100 °C (2.5 °C/min). Gas concentrations including NH_3 (m/z = 17), N_2 (m/z = 28), H_2 (m/z = 2), and Ar (m/z = 40) were detected by mass spectrometer. The experiments were conducted under 1.0 atm.

Computational details

DFT calculations were performed using the Vienna ab initio simulation package (VASP) to investigate the synergy between Co and Ni as well as between the metals and supporting oxides in the catalysts, [5, 6] The Perdew−Burke−Ernzerhof (PBE) functional[7] and the Projector Augmented Wave (PAW)[8] potentials were used with a plane wave basis set of 450 eV cut-off energy. The Brillion zone was sampled with a (3 × 3 × 1) k-point grid for the metal surfaces modeled using a 4-layer slab and a p(3 × 3) surface cell (**Figure S27**). The effect of support was modeled using a ledge of CeO_2 on a 4-layer Co_2Ni slab of $(3 \times 3\sqrt{3})$ and sampled with a (3 × 2 × 1) k-point grid (**Figure S28**). A vacuum gap of 15 Å was added to minimize interaction between the periodic images along the direction perpendicular to the surface. Geometry optimizations were performed using the Quasi-Newton algorithm[9] with a convergence criterion of 10^{-4} eV. The atoms in the top two layers of the slab, and those of CeO_2 in the case of the supported system, were allowed to relax while the atoms in the bottom two layers were fixed in the corresponding bulk positions. Transition states were determined using a combination of the Quasi-Newton algorithm[9] and the dimer method[10] and were confirmed by frequency analysis. Similar setup and parameters have been used in our previous studies, including ammonia synthesis and decomposition. The adsorption energy was calculated as:

$$E_{ads} = E_{adsorbate/slab} - E_{adsorbate} - E_{slab}$$

$E_{adsorbate/slab}$, $E_{adsorbate}$, and E_{slab} are the total energies of the species adsorbed on the slab, the isolated adsorbate, and the clean slab, respectively. The relaxed fcc bulk structures of pure Ni and Co and alloys with Co:Ni ratios of 2:1 and 1:2 was used to construct the corresponding slab for ammonia adsorption and dissociation. Binding energies of NH_x on different surface sites, elementary dissociation steps of the adsorbed NH_x species, and H_2 and N_2 formation have been calculated. Our results for ammonia and intermediate adsorption on Co (111) and Ni (111) agree with the previous report,[11] confirming that the models and parameters used in the present study are adequate.

Additional figures and tables

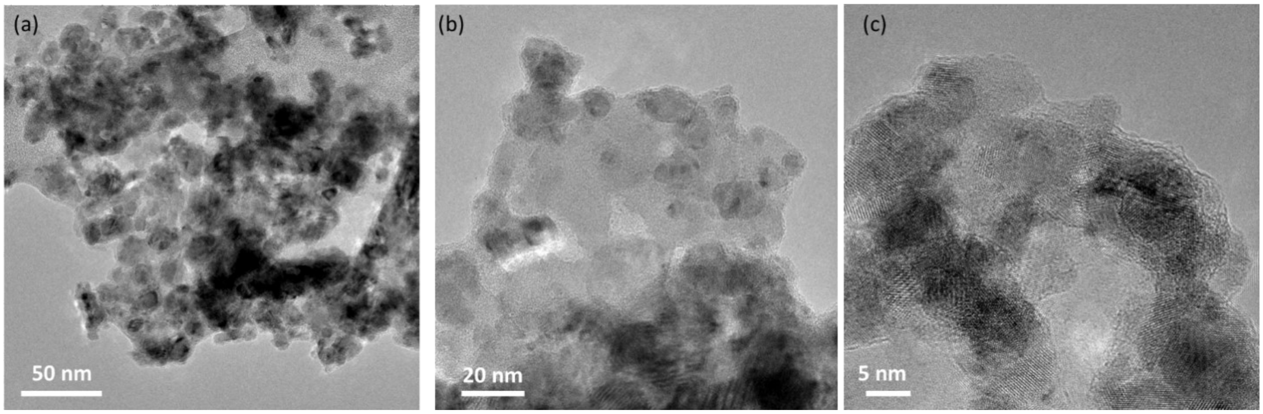

Figure S1. TEM images of the K-$CoNi_{alloy}$-MgO-CeO_2-SrO catalyst at different magnifications. (a) scale bar 50 nm, (b) scale bar 20 nm, and (c) scale bar 5 nm.

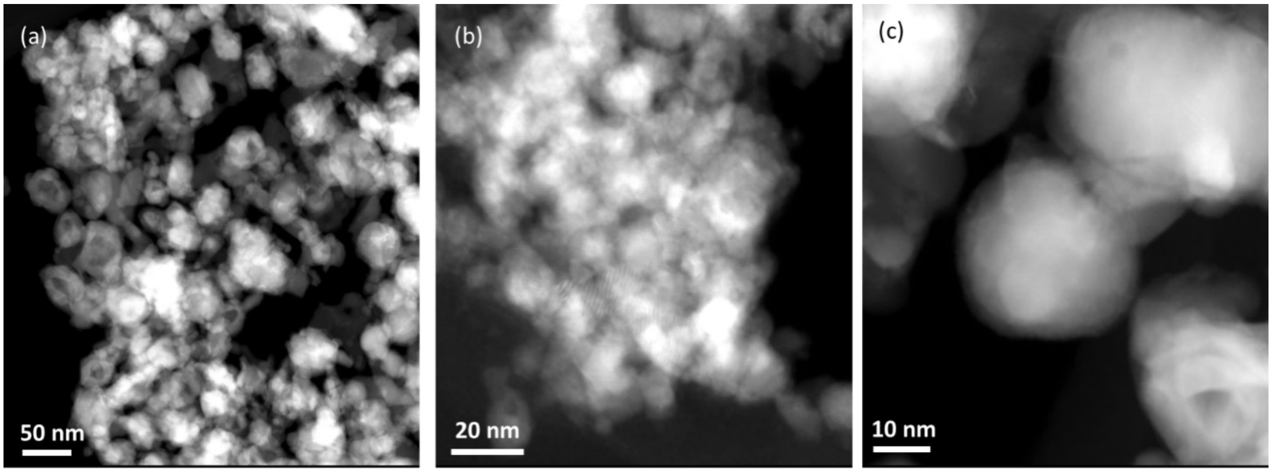

Figure S2. HAADF-STEM images of K-$CoNi_{alloy}$-MgO-CeO_2-SrO at different magnifications.

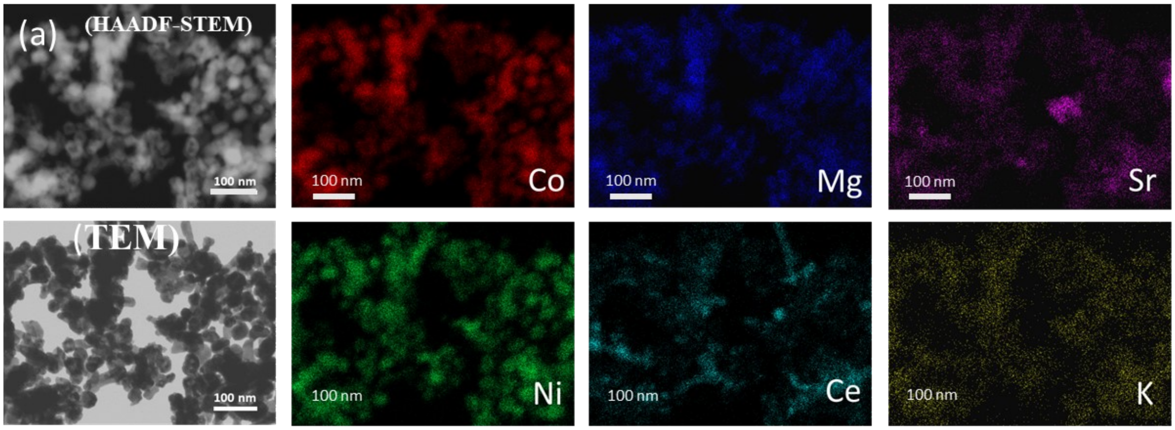

Figure S3. (a) Low magnificationTEM, HAADF-STEM and elemental mapping of K-CoNi$_{alloy}$-MgO-CeO$_2$-SrO along with elemental mapping.

A small content of K exists in the atomic form in heterostructure ADR catalysts. The K acts as an electron-donating element on the surface of the catalyst which can affect the electronic properties of the supported metals and boosts the activity of ADR catalysts. The HAADF-STEM mapping of K-CoNi$_{alloy}$-MgO-CeO$_2$-SrO catalyst at scale bars 100nm (**Figure S3**) and (**FigureS4)** 10 nm clearly showed the uniform dispersion of K in the catalyst.

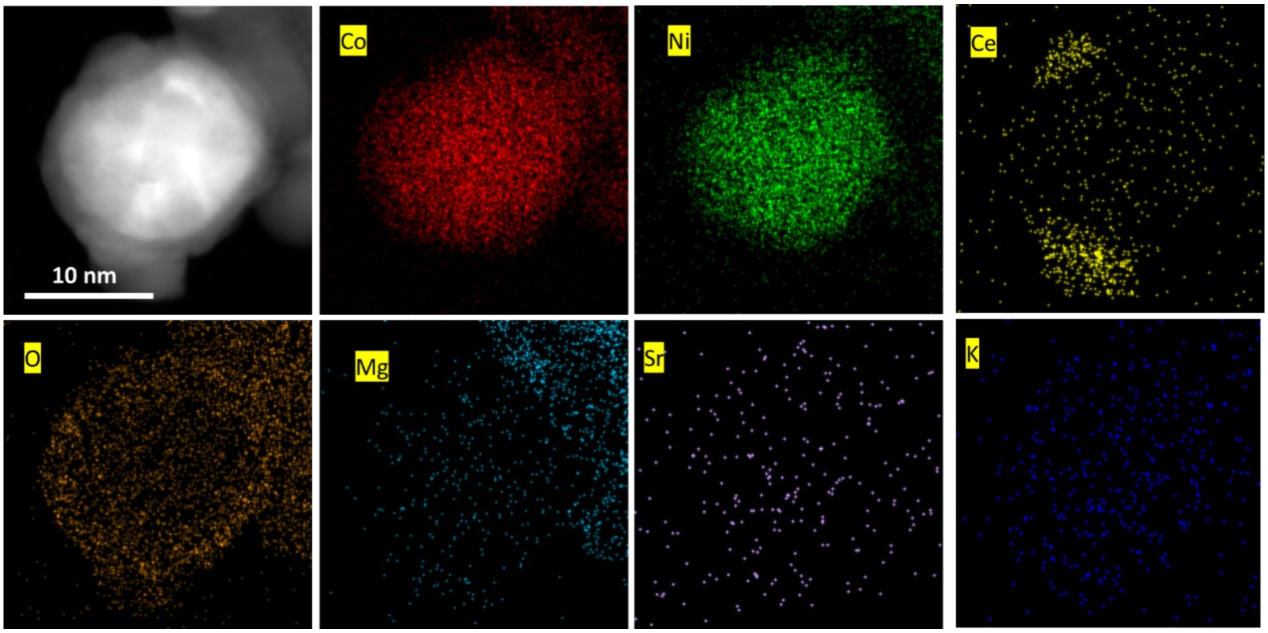

Figure S4. HAADF-STEM images and EDS elemental maps of the K-CoNi$_{alloy}$-MgO-CeO$_2$-SrO catalyst. Scale bar 10 nm and corresponding elemental mapping.

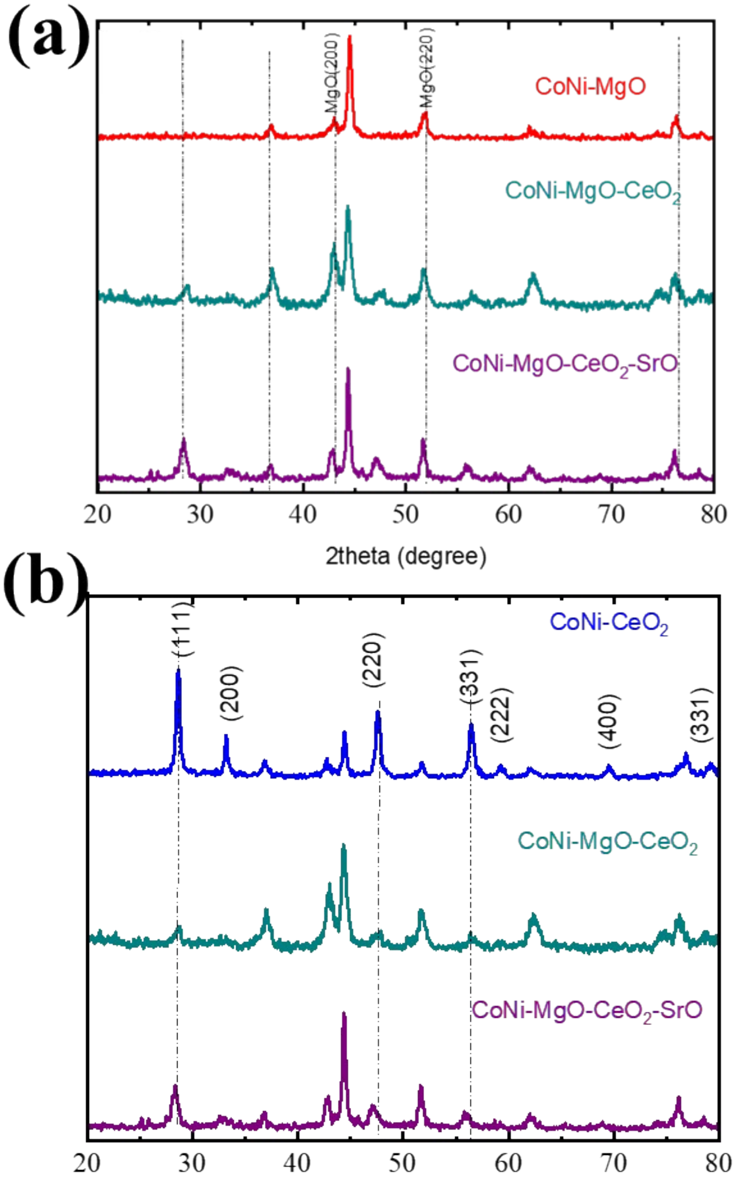

Figure S5. (a) XRD patterns of the CoNi-MgO, CoNi-MgO-CeO$_2$, CoNi-MgO-CeO$_2$-SrO catalysts, and (b) XRD patterns of the CoNi-CeO$_2$, CoNi-MgO-CeO$_2$, CoNi-MgO-CeO$_2$-SrO catalysts.

For all studied samples, no prominent peaks are related to SrO, indicating that the Sr ions are effectively incorporated into the MgO and CeO$_2$ lattices to form mixed oxide. Besides, no peaks associated with K or K$_2$O were detected in XRD patterns which support the atomic dispersion of K in catalysts. A slight shift was observed for MgO (200) and (220) in the mixed oxide supported CoNi catalysts (*e.g.*, MgO-CeO$_2$ and MgO-CeO$_2$-SrO), compared to individual MgO (**Figure S5a**). Also, a similar observation was for the CeO$_2$ (220) in the MgO-CeO$_2$-SrO supported CoNi catalyst (**Figures S5b** and **S6a**), which is likely due to the slight doping of Mg or/and Sr into CeO_2 which supports the mixed oxide support structure.

Tables S1 and **S2** summarized surface areas, pore size distribution, pore-volume, active site density (determined by using CO uptake), CoNi crystalline size, and the corresponding NH_3 conversion for all studied catalysts. Crystallite sizes were calculated for the CoNi alloy using the Scherrer equation from XRD patterns based on (111), (200), and (220) planes at 44.32°, 51.62°, and 76.16°, respectively. CoNi alloy crystallites (~11 nm) were found smaller than individual Co or Ni (~14 nm) ones (**Table S1**). For the optimal K-promoted support, the smallest crystallite size of CoNi alloy was found to be the least (8.74 nm) (**Table S2**), generating increased active sites and promoting the ammonia decomposition activity.[12-14] Notably, the K-promoted catalyst has a relatively low active site density (based on CO pulse chemisorption) but presents the highest catalytic activity. Generally, adding K plays two essential roles in promoting NH_3 decomposition. As evidenced by XRD patterns, the first role is to improve metal particle dispersion by reducing CoNi alloy crystallite sizes. The reduced sizes can create significantly increased interfaces of CoNi alloy particles and oxides in the catalysts.

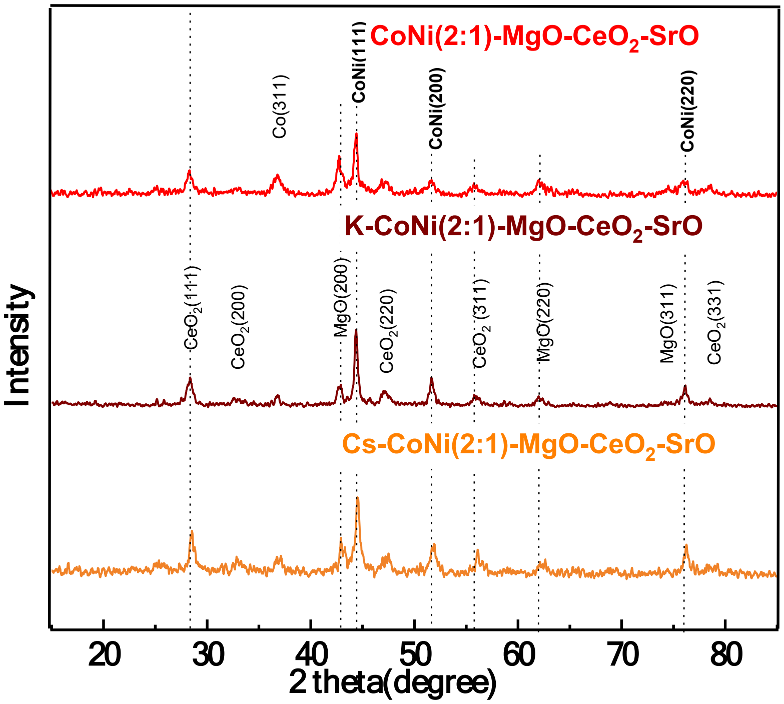

Figure S6. XRD patterns of the CoNi(2:1)-MgO-CeO_2-SrO, K-CoNi(2:1)-MgO-CeO_2-SrO and Cs-CoNi(2:1)-MgO-CeO_2-SrO catalysts,

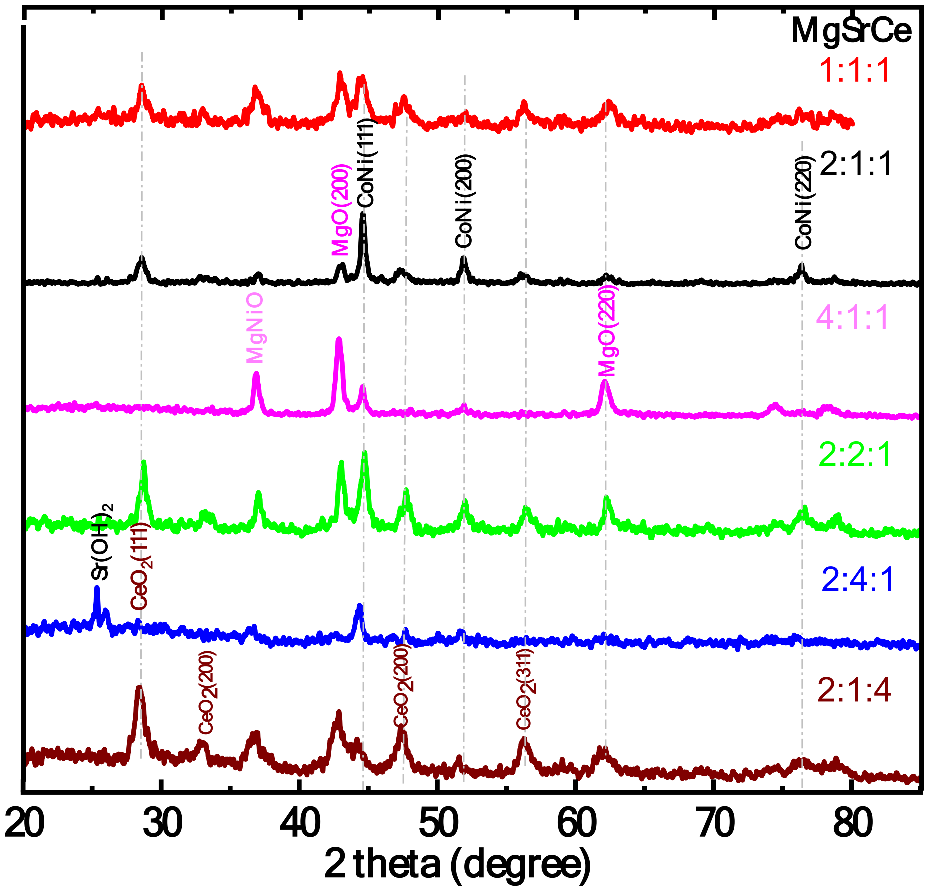

Figure S7. XRD patterns of K-CoNi alloy catalysts supported on ternary mixed oxides with various Mg: Sr: Ce ratios. In particular, $Sr(OH)_2$ was observed for the catalyst with high Sr content (Mg: Sr: Ce = 2:4:1) (**Figures S7** and **S8c**). In contrast, for the optimal Mg: Sr: Ce ratio (*i.e.*, 2:1:1)

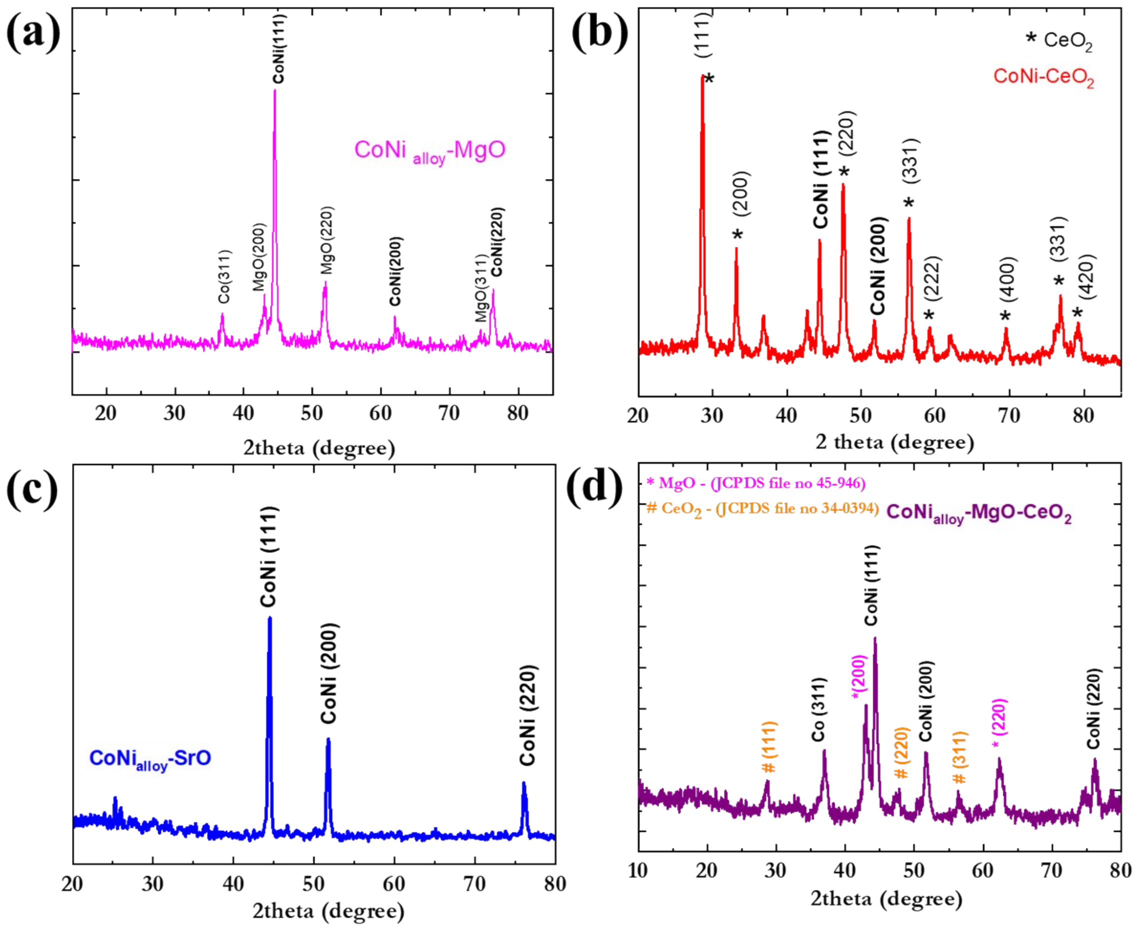

Figure S8. XRD patterns for (a) the $CoNi_{alloy}$-MgO, (b) the $CoNi_{alloy}$-CeO_2, (c) the $CoNi_{alloy}$-SrO, and (d) the $CoNi_{alloy}$-MgO-CeO_2 catalysts.

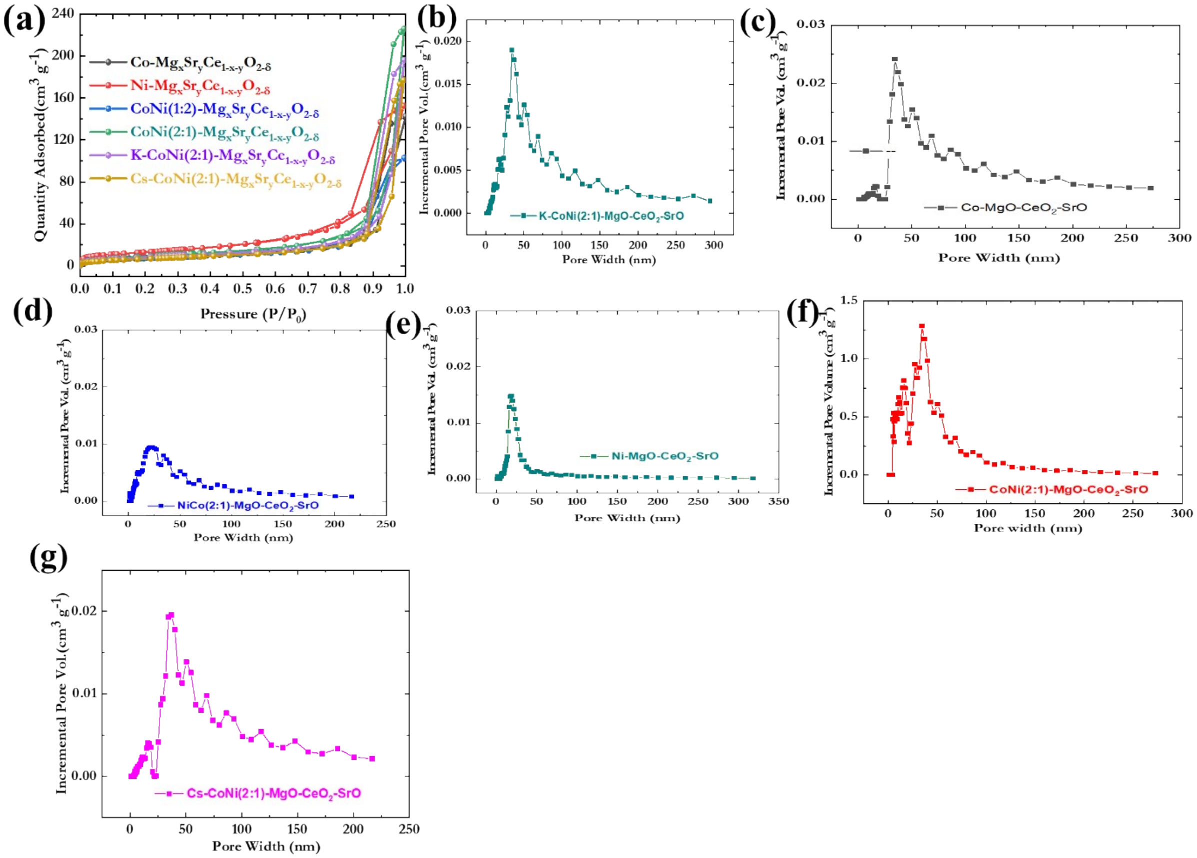

Figure S9. (a) N_2 adsorption/desorption isotherm curves, and (b-g) Pore size distribution for the catalysts.

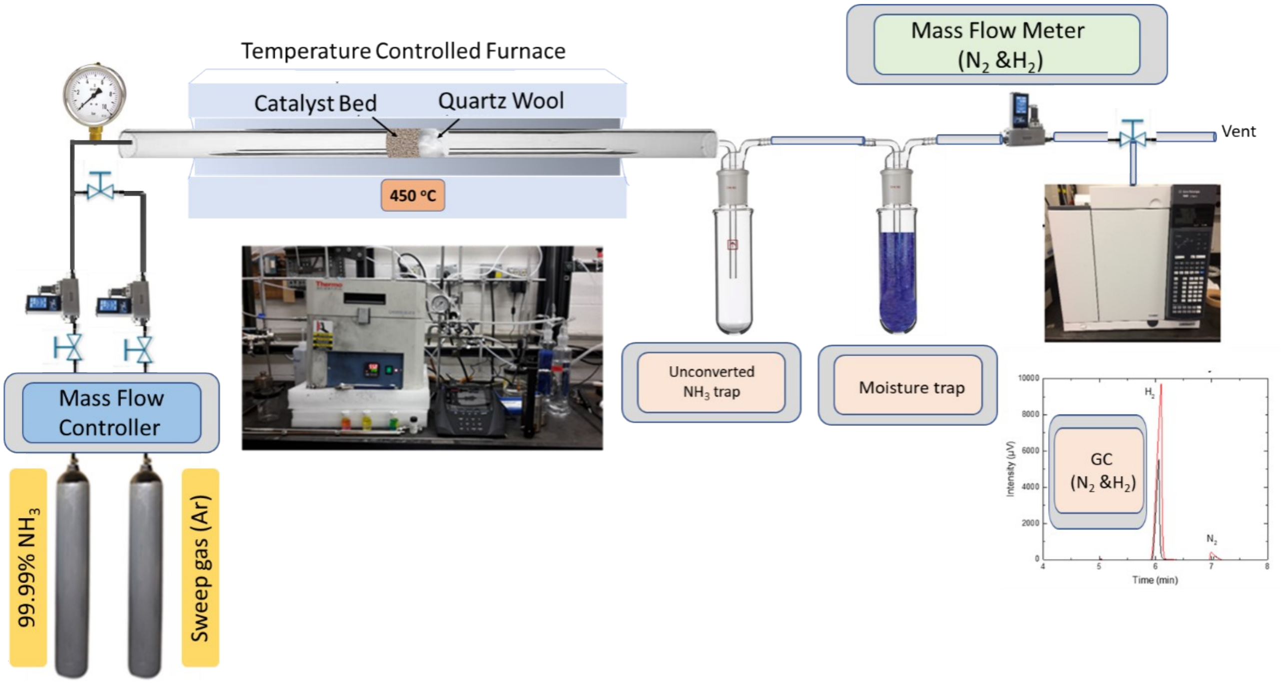

Figure S10. A schematic of micro-reactor set up for testing catalysts, including the moisture trap to prevent corrosion from strong acid fumes.

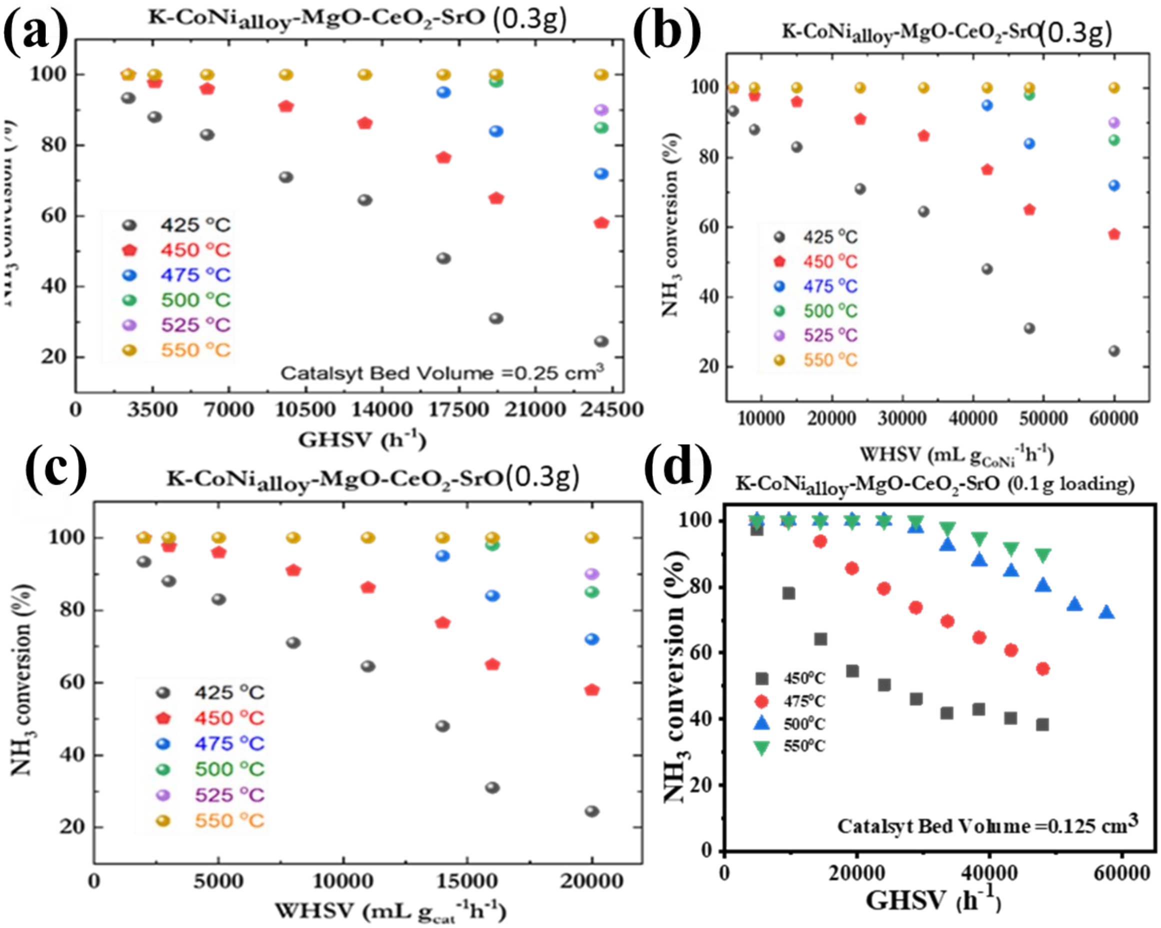

Figure S11. NH_3 decomposition efficiencies at different increasing space velocity values, measured with respect to (a) catalyst bed volume (b) total weight of catalyst loaded and (c) active metal loading in mL g_{CoNi}^{-1} min^{-1}, represented in h^{-1}, mL g_{cat}^{-1} h^{-1}, mL $g_{CoNi}^{-1}h^{-1}$, respectively. (d) small catalyst bed volume with 0.1g mass loading.

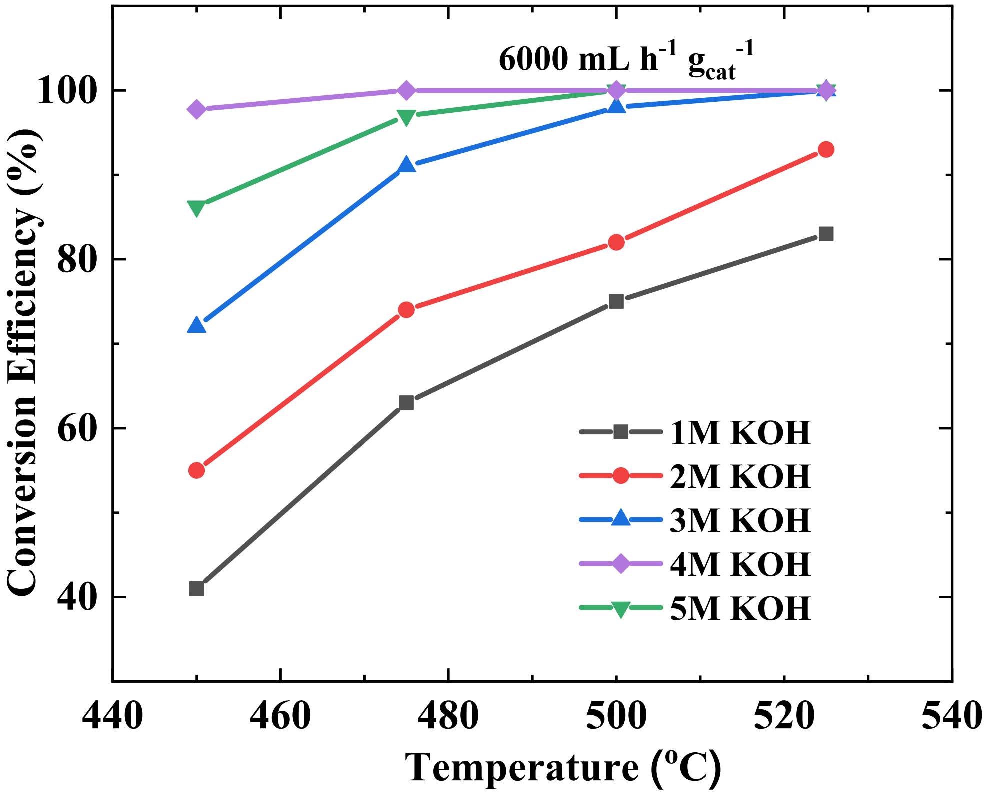

Figure S12. (The K-promoter effect was found by using different molarity of KOH (1M, 2M, 3M, 4M and 5M) for ADR conversion efficiency of K-CoNi$_{alloy}$-MgO-CeO$_2$-SrO, The catalyst presented 41%, 55%, 72%, 97.75 and 86.2% at 1MKOH, 2MKOH, 3M KOH, 4MKOH and 5M KOH, respectively.

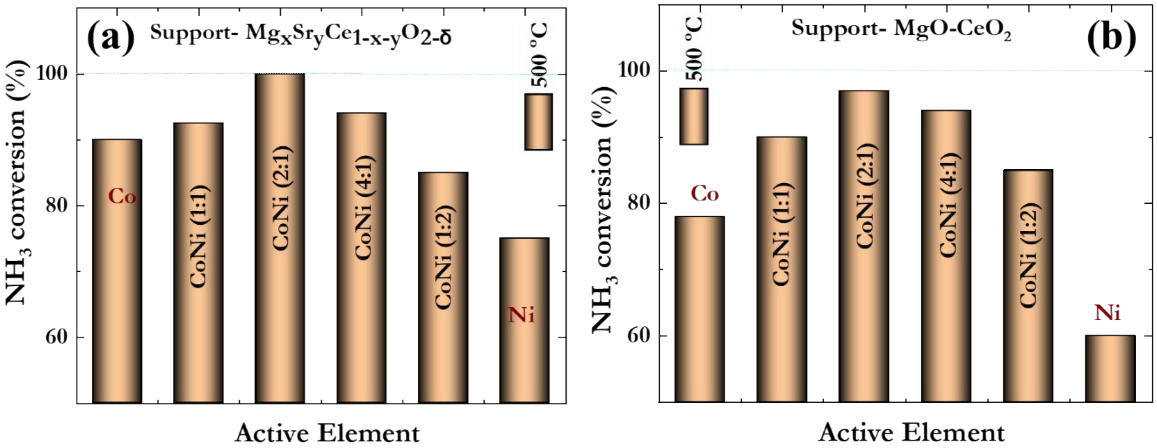

Figure S13. NH_3 decomposition activity for different ratios of Co and Ni K-CoNi$_{(1:1)}$-MgO-CeO_2-SrO, K-CoNi$_{(4:1)}$-MgO-CeO_2-SrO and K-CoNi$_{(1:2)}$-MgO-CeO_2-SrO , mono-metal with support oxides Co-MgO-CeO_2-SrO(90%) catalyst performed better than the Ni-MgO-CeO_2-SrO(75%) at 500 °C supported on (A) the MgO-CeO_2-SrO and (B) the MgO-CeO_2 support.

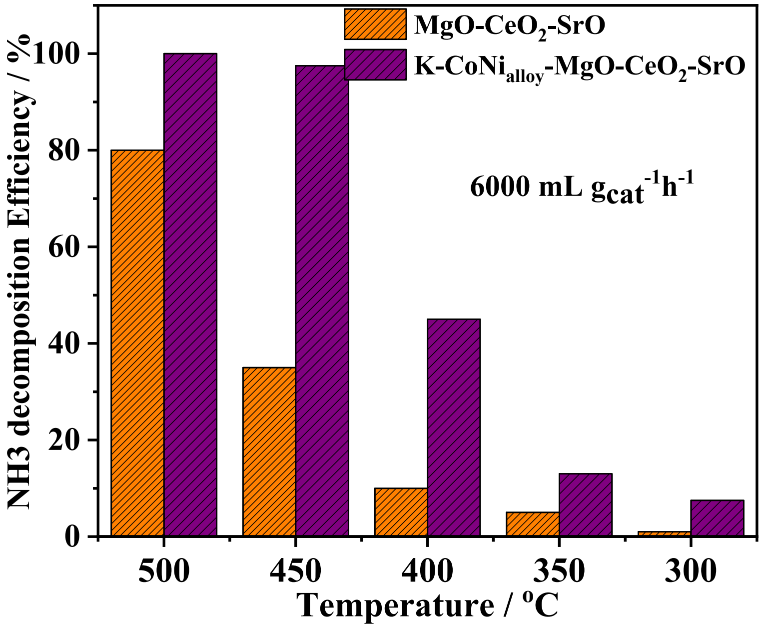

Figure S14. ADR activity comparison of Support (MgO-CeO_2-SrO) and highly performed K-CoNi$_{alloy}$-MgO-CeO_2-SrO catalyst.

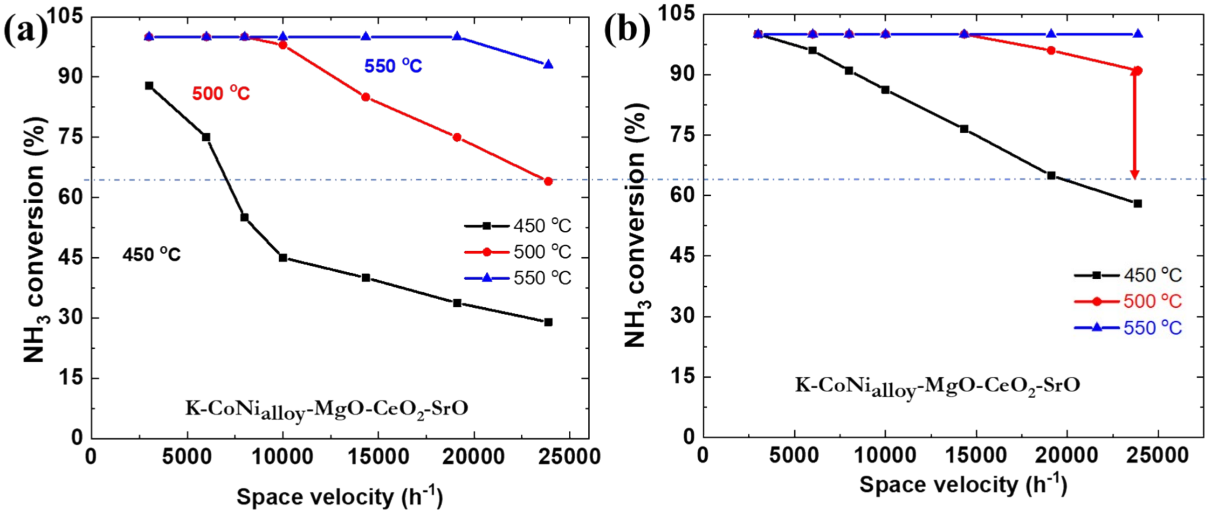

Figure S15. NH_3 decomposition efficiency with increasing space velocity at different temperatures for the K-$CoNi_{alloy}$ catalysts supported on various supports. (a) MgO-CeO_2 (b) MgO-CeO_2-SrO.

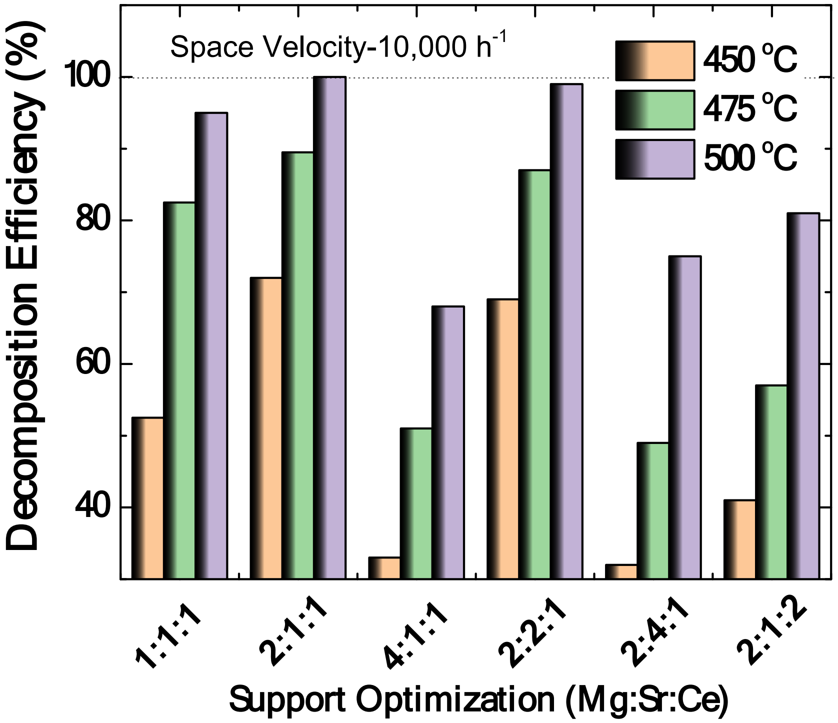

Figure S16. Effect of molar ratios of Mg, Sr, and Ce in the mixed oxide support on the NH_3 decomposition efficiency of K-$CoNi_{alloy}$ catalysts.

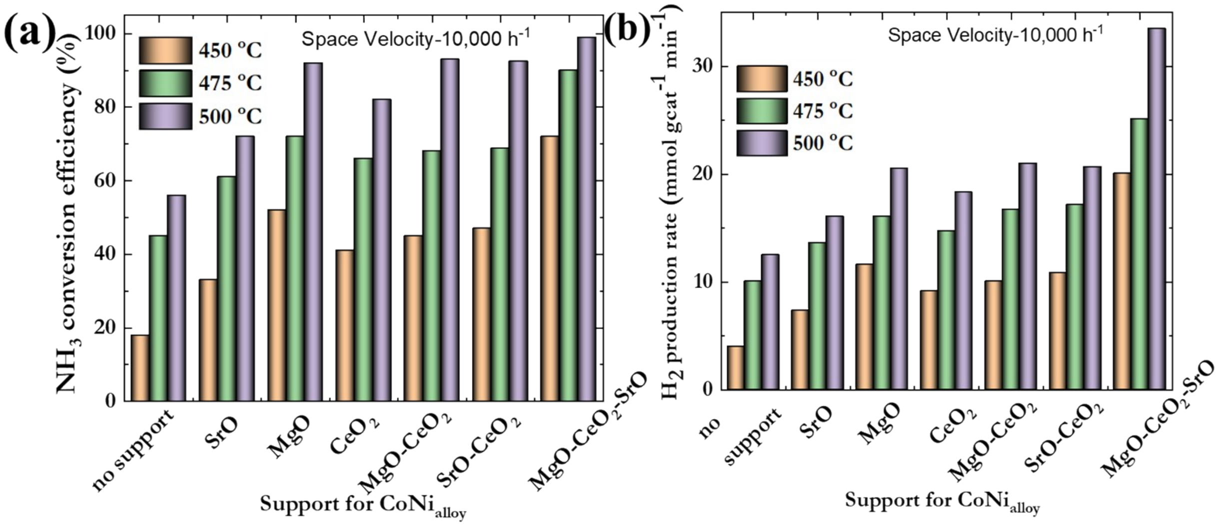

Figure S17. Comparisons of (a) NH_3 decomposition efficiencies and (b) H_2 production rates of $CoNi_{alloy}$ catalysts supported on different supports.

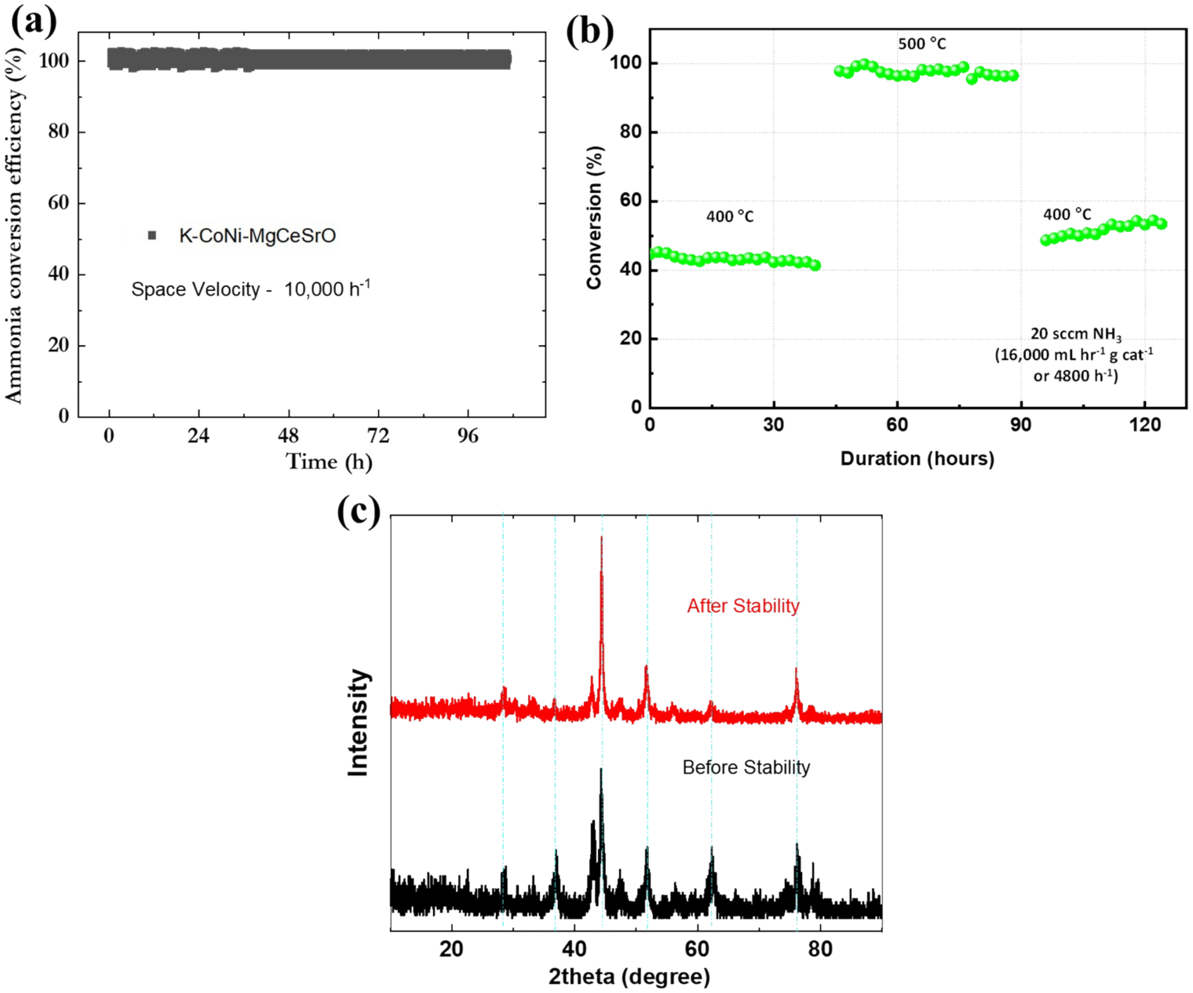

Figure S18. (a) Stability test of the K-CoNi$_{alloy}$-MgO-CeO$_2$-SrO catalyst in a fixed bed reactor at 500 °C for 100 h. (b) Stability test at 400 °C with a conversion efficiency close to 50%, showing good stability. The activity is slightly enhanced after switching to 500 °C for 40 hours and then back to 400 °C. (c) XRD patterns of the catalyst before and after the stability test.

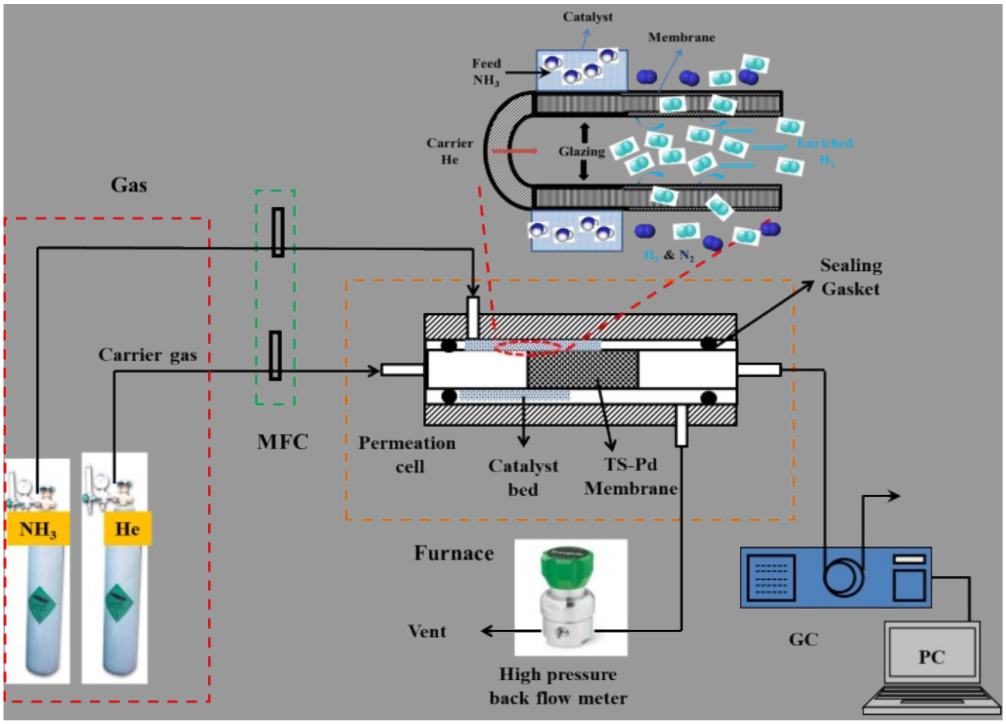

Figure S19. A schematic of a prototype membrane reactor setup for testing catalyst stability.

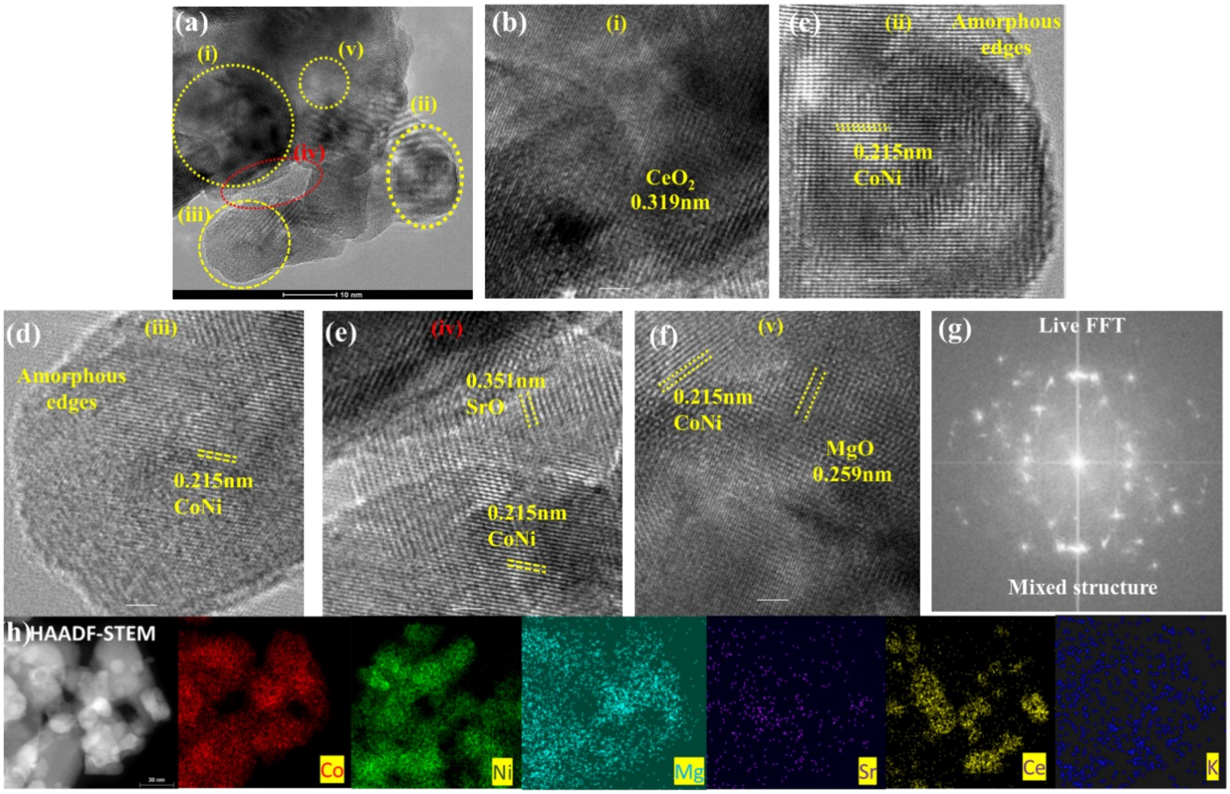

Figure S20. (a) HRTEM of and HAADF-STEM mapping of K-CoNi$_{alloy}$-MgO-CeO$_2$-SrO catalyst after 600h Stability test at 500 °C with pure NH$_3$ over K-CoNi$_{alloy}$-MgO-CeO$_2$-SrO with a GHSV of mL h^{-1} g$_{cat}$$^{-1}$ at 1.5 bar.

The mixed oxide support is surrounded by CoNi alloy (0.215nm)and presented defined interlayer spacing of MgO (0.259nm), CeO2(0.319nm,) and SrO(0.351nm). The live Fast Fourier Transform (FFT). The mixed oxide support is surrounded by CoNi alloy (0.215nm) and presented defined interlayer spacing of MgO (0.259nm), CeO2(0.319nm,) and SrO(0.351nm), edges of the few CoNi$_{alloy}$ particles exhibited amorphous structure (**Figure S20 b-g**). The live Fast Fourier Transform (FFT) also exhibited the disorder's bright spots to show the multimetal interface (**Figure S20g**). The HAADF-STEM elemental mapping also presented the uniform distribution of multielement nanoparticles (**Figure S20h**). Based on this evidence, we believed that the mixed oxide surrounding the CoNi alloy nanoparticles can act as spacers to prevent them from sintering

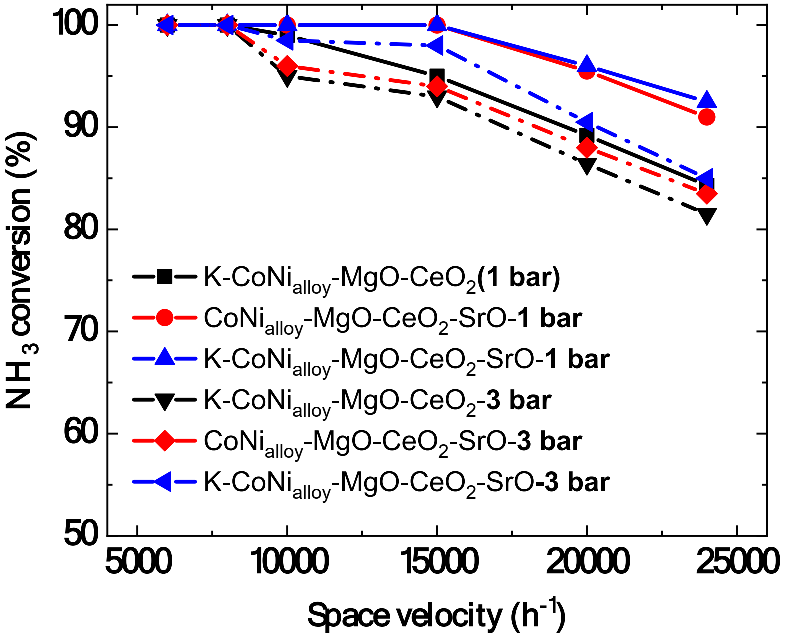

Figure S21. Effect of operating pressures on the catalytic activity at 500 ^{o}C in fixed bed reactor for the K-CoNi$_{alloy}$-MgO-CeO$_2$, CoNi$_{alloy}$-MgO-CeO$_2$-SrO, and K-CoNi$_{alloy}$-MgO-CeO$_2$-SrO catalysts.

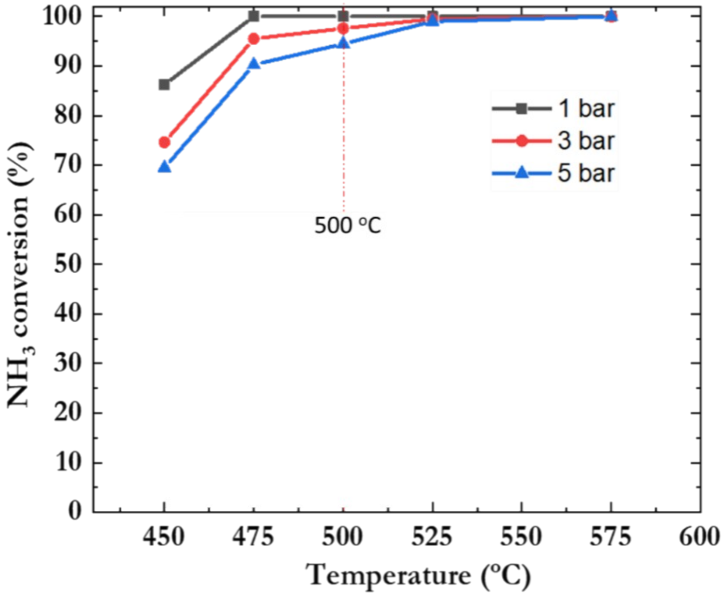

Figure S22. NH_3 conversion efficiencies at different operating pressures and temperatures for the best performing K-$CoNi_{alloy}$-MgO-CeO_2-SrO catalysts. Space velocity (10,000 h^{-1}, GHSV = 24,000 mL g_{CoNi}^{-1} h^{-1}).

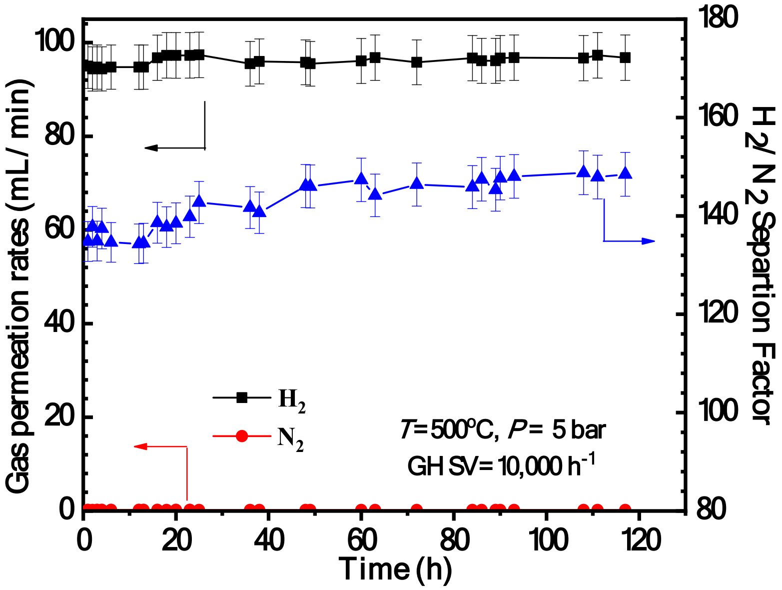

Figure S23. Stability test of the K-$CoNi_{alloy}$-MgO-CeO_2-SrO catalyst in a prototype membrane reactor at 500 °C and 5.0 bar at GHSV of 10,000 h^{-1}.

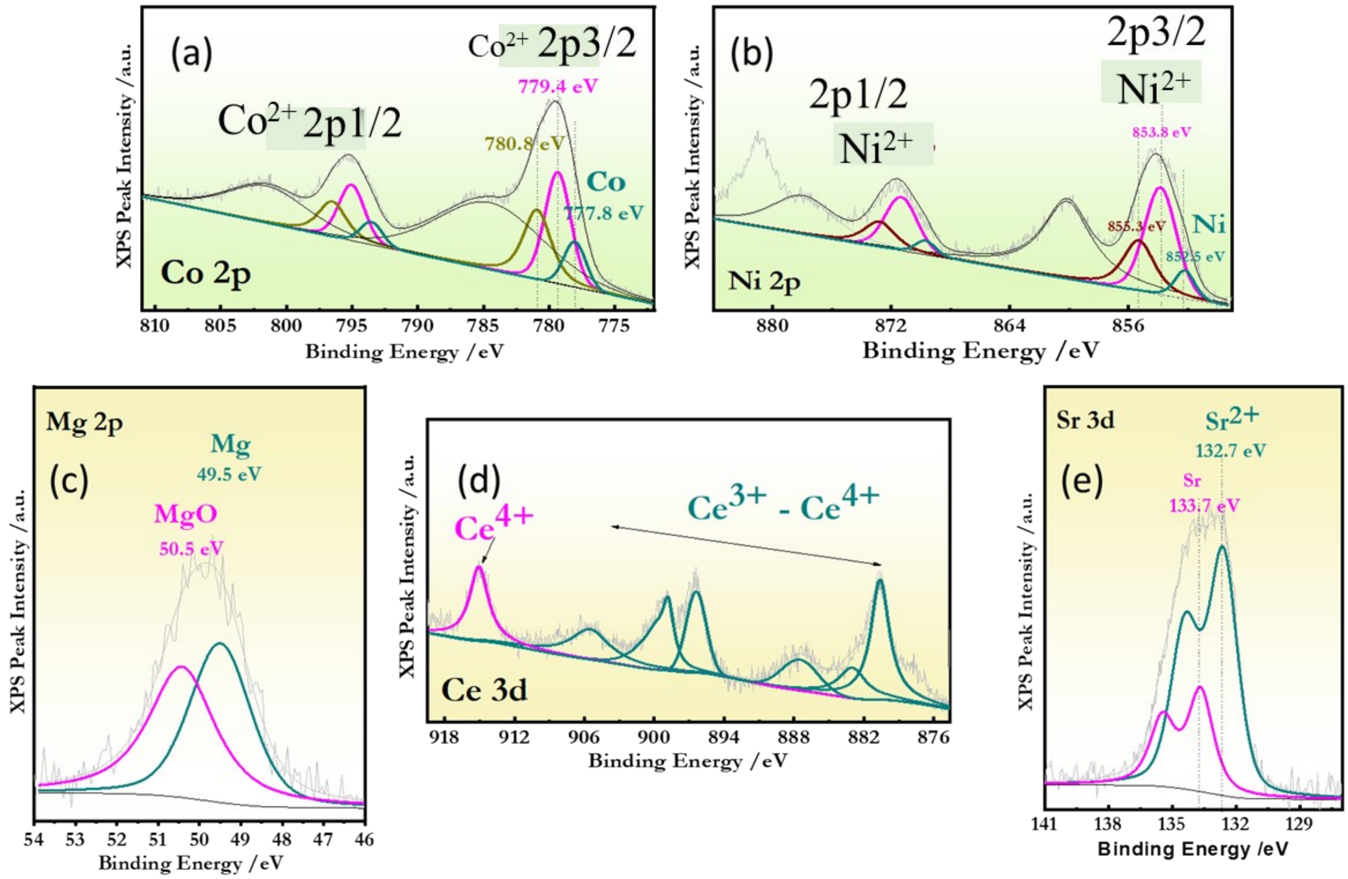

Figure S24. Conventional *ex-situ* XPS analysis for the best performing K-$CoNi_{alloy}$-MgO-CeO_2-SrO catalyst. (a) Co 2p, (b) Ni 2p, (c) Mg 2p, (d) Ce 3d, and (e) Sr 3d.

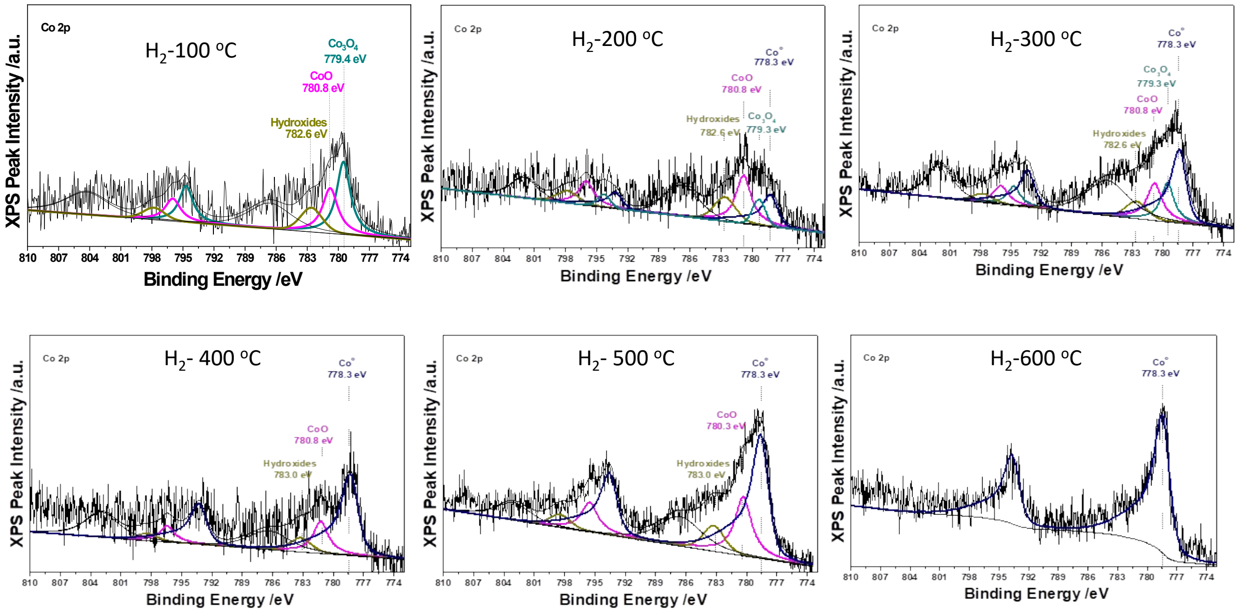

Figure S25. A comparison of *in-situ* XPS analysis of Co 2p when reduced in pure H_2 at temperatures from 100 to 600 °C.

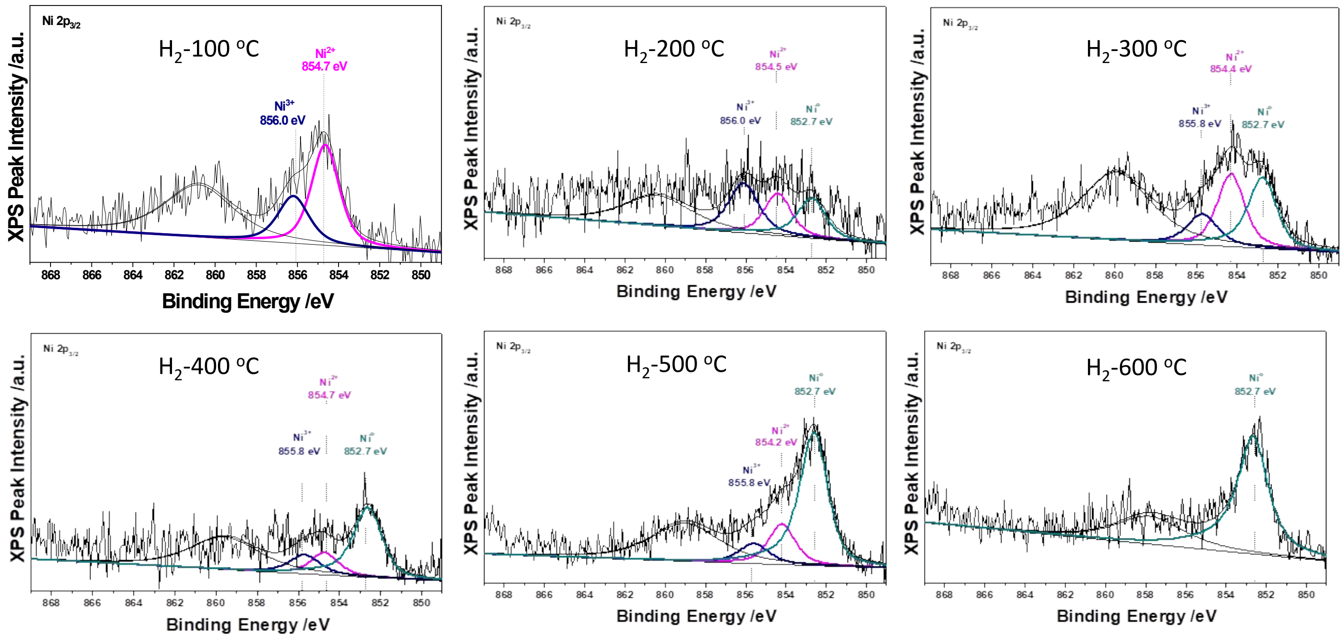

Figure S26. A comparison of *in-situ* XPS analysis of Ni 2p when reduced in pure H_2 at temperatures from 100 to 600 °C.

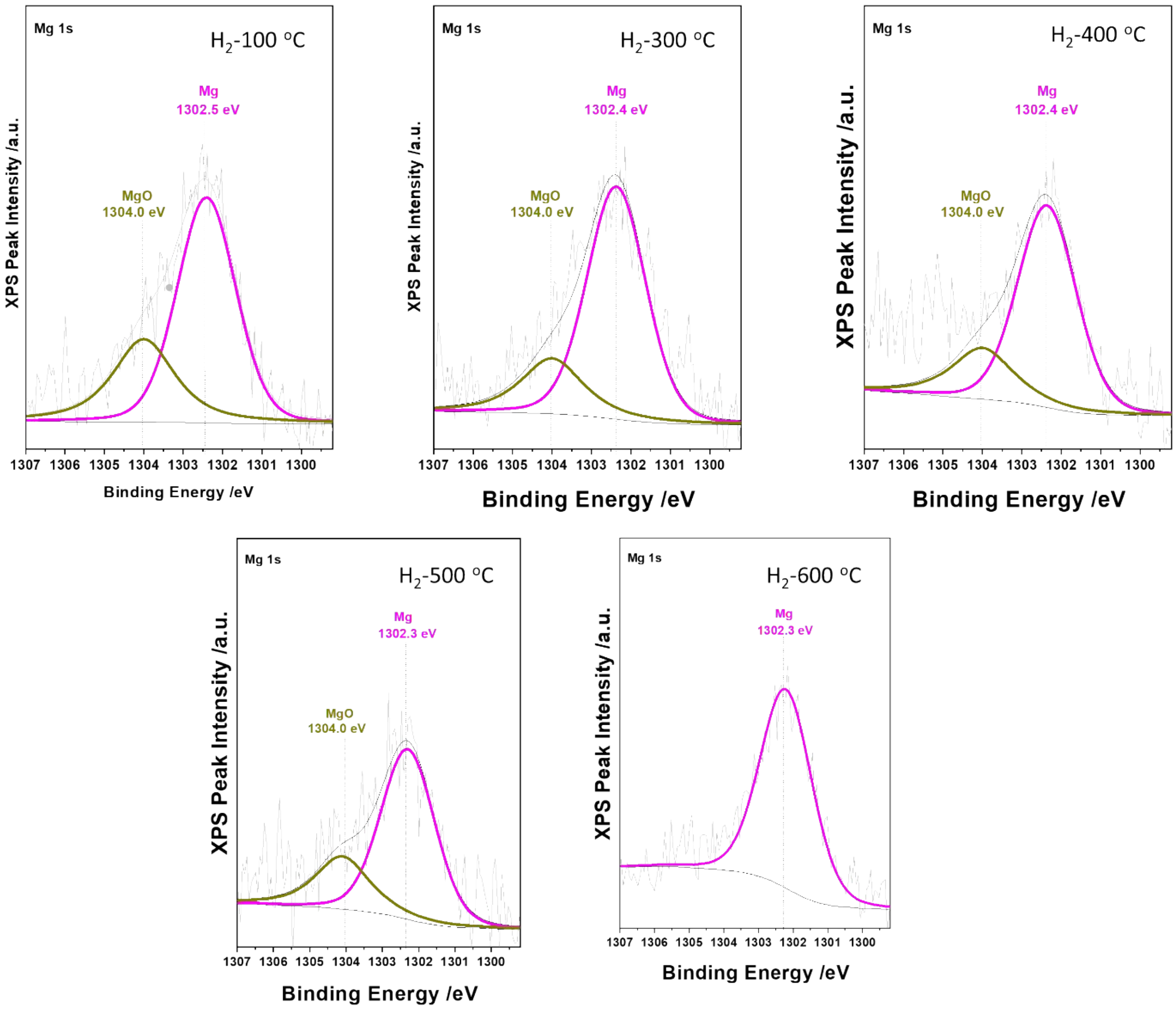

Figure S27. A comparison of *in-situ* XPS analysis of Mg 1s when reduced in pure H_2 at temperatures from 100 to 600 °C.

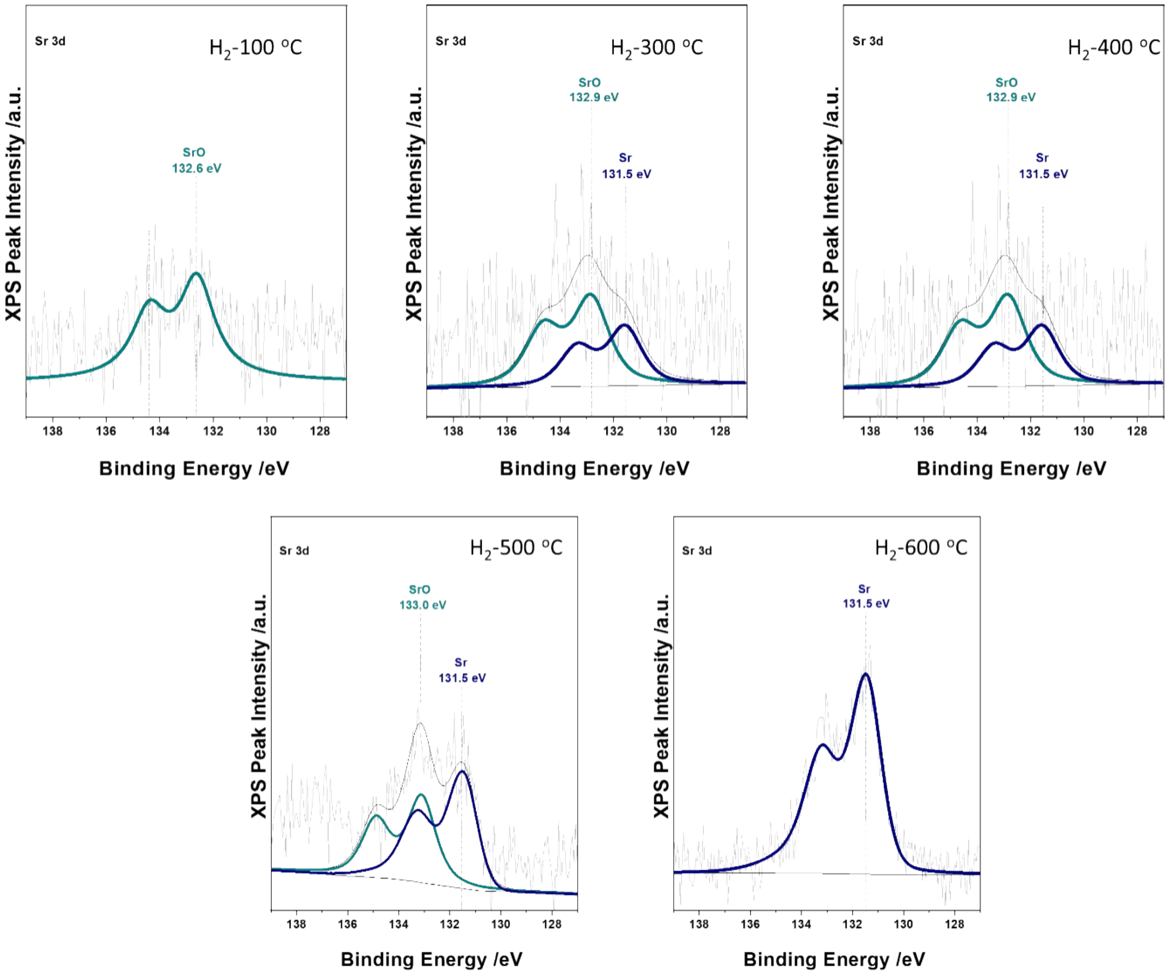

Figure S28. A comparison of *in-situ* XPS analysis of Sr 3d when reduced in pure H_2 at temperatures from 100 to 600 ^{o}C. The in-situ high-temperature The XPS spectra after exposing the catalyst to temperatures between 100 and 600 ^{o}C in pure H_2, The deconvoluted XPS 3d orbital level into two orbitals of Sr3d$_{5/2}$ and Sr 3d$_{3/2}$ at binding energies of 132.2 and 135.1 eV respectively with a spin separation of 2.9eV, at high temperatures (500°C). The doublet separation (Sr3d$_{5/2}$-3d$_{3/2}$) is greater than 1.79eV(Sr metallic), confirming the oxidation state of Sr.

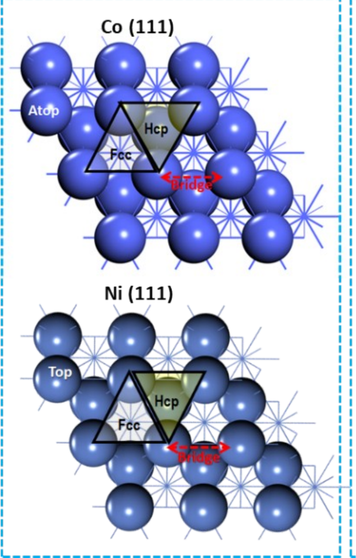

Calculated binding energies of NH_X sites on Co and Ni vs reference

Co	This study	**Reference	sites
NH	-4.65	-4.63	hcp
N	-5.58	-5.53	hcp
H	-2.76	-2.77	fcc

Ni	This study	Reference**	sites
NH_3	-0.75	-0.75	top
NH_2	-2.73	-2.73	bridge
NH	-4.60	-4.57	fcc
N	-5.33	-5.30	fcc
H	-2.80	-2.81	hcp

Calculated *NH dissociation and N_2 formation on Co vs reference

Co		This study	**Reference
NH -> N + H	E_r	0.17	0.10
	E_a	1.09	1.06
N_2 formation	E_r	0.64	0.62
	E_a	1.62	1.86

Figure S29. Adsorption sites and calculated adsorption energy of NH_x on Co and Ni. The results are compared with results reported in ref.[8]

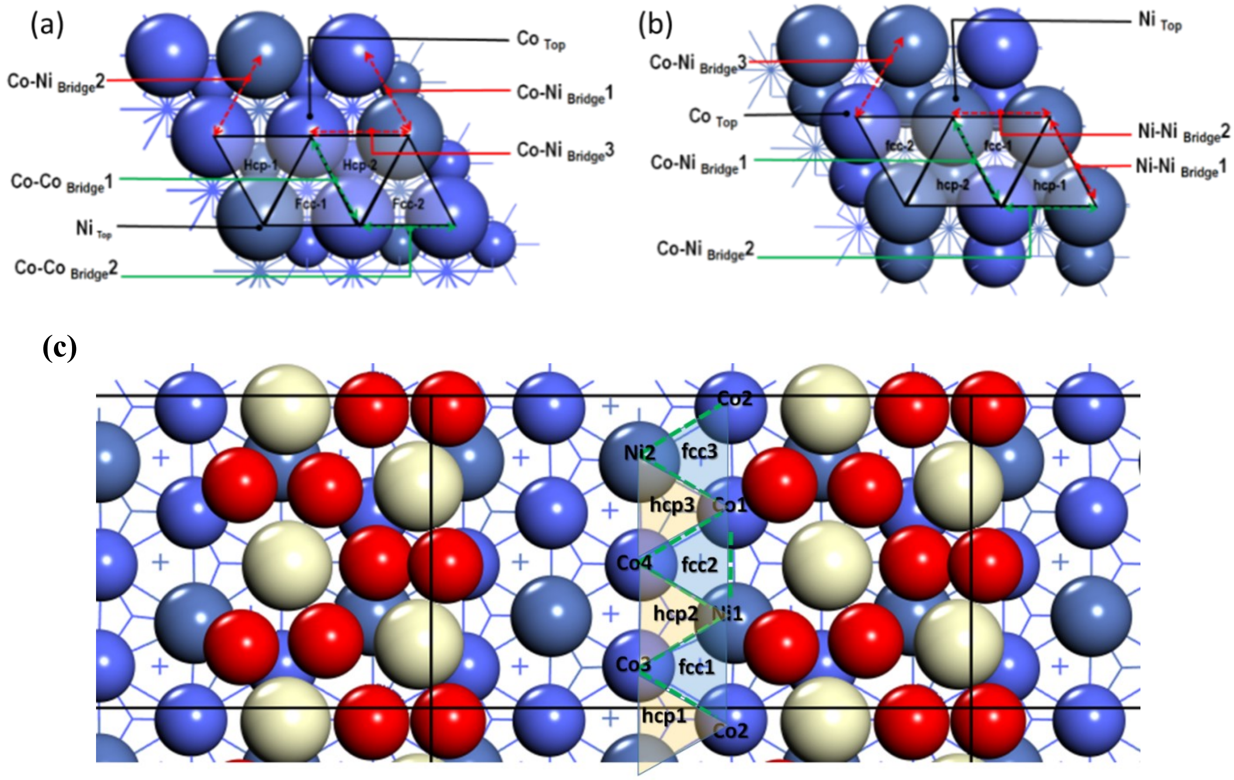

Figure S30 Top view of unit cells of (A) Co_2Ni (111) surface and (B) $CoNi_2$ (111). Blue and dark cyan balls represent Co and Ni, respectively. The atoms in the top layer are represented with larger balls, while the atoms in the two bottom layers are represented by lines. (C) CeO_2 supported on the Co_2Ni (111) surface. Blue, dark cyan, red, and yellow balls represent Co, Ni, O, and Ce. The atoms in the top layer are represented with balls, while the atoms in the sublayer are represented by lines and the bulk atoms by crosses.

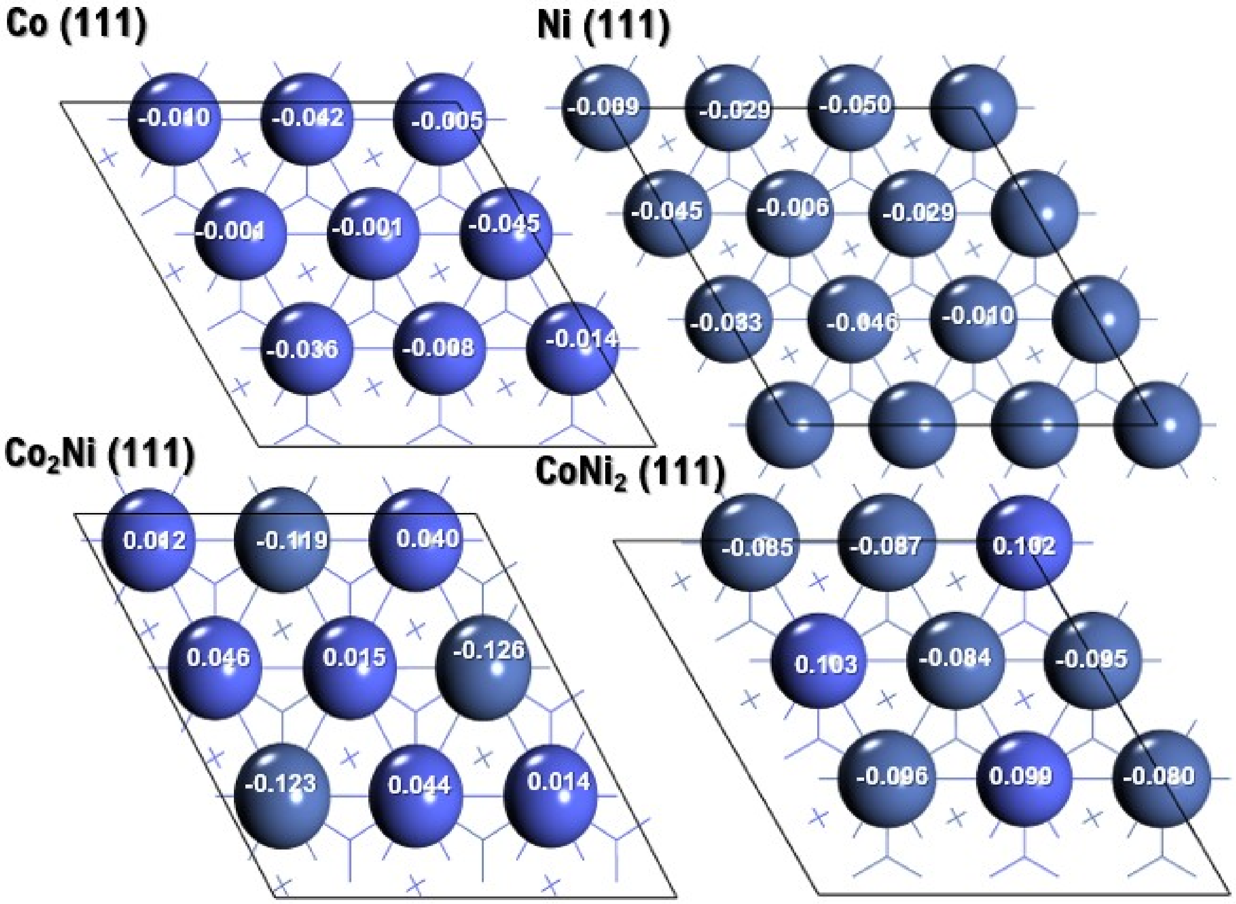

Figure S31. Top view of the surface unit cells of the metals. Also shown are the Badger charge values of the surface metal atoms.

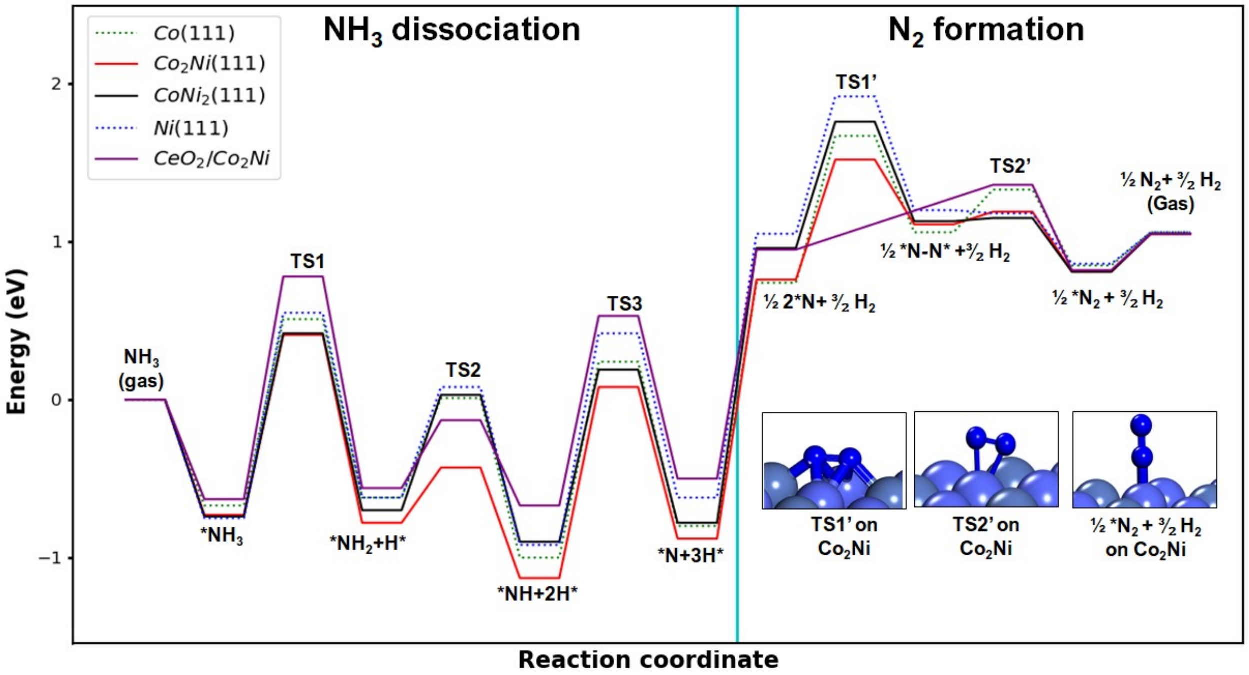

Figure S32. The energy profiles of NH_3 dissociation and N_2 formation on Co (dotted green line), Co_2Ni (red line), $CoNi_2$ (black line), Ni (dotted blue line), and CeO_2/Co_2Ni (purple line) surfaces. Values for NH_3 dissociation on pure Co and Ni were obtained from reference 8.

Table S1. A summary of CoNi alloy crystallite size with varying ratios of the moles of individual elements in the support precursor.

Mg:Sr:Ce Ratio	CoNi phase	2theta (degree)	Crystallite size (nm)
2:1:1	111	44.42	8.74
2:1:2	111	44.42	14.29
2:1:4	111	44.42	15.69
2:2:1	111	44.42	10.24
2:4:1	111	44.42	13.69
4:1:1	111	44.42	15.62

Table S2. Comparisons of surface area, pore-volume, CO pulse chemisorption results, and CO_2-TPD peak areas for the Co, Ni, CoNi(1:2), CoNi(2:1), K-CoNi(2:1), and Cs-CoNi(2:1) based catalysts supported by the ternary mixed oxide support.

Samples	BET surface area (m^2 g^{-1})	Pore volume (cm^3 g^{-1})	CO uptake (µmol/g)[a]	Active Metal Crystallite Size (nm)[b]	CO_2 TPD peak area (a.u)	NH_3 conversion at 450 °C (GHSV = 10,000 h^{-1})
Co-MgO-CeO_2-SrO	18.6	0.132	25.1	13.7	0.033	54.6
Ni-MgO-CeO_2-SrO	8.7	0.111	22.1	14.0	0.016	31.0
CoNi(1:2)-MgO-CeO_2-SrO	26.1	0.164	33.2	14.2	0.024	58.9
CoNi(2:1)-MgO-CeO_2-SrO	34.1	0.505	109.8	11.5	0.037	83.3
K-CoNi(2:1)-MgO-CeO_2-SrO	30.2	0.264	64.8	8.74	0.061	91.6
Cs-CoNi(2:1)-MgO-CeO_2-SrO	25.2	0.157	88.1	11.7	0.057	88.1

[a] CO uptake was calculated from the CO pulse chemisorption at 35 °C

[b] Calculated from XRD using Scherrer equation

Table S3. A summary of Ru-based catalyst for hydrogen generation from NH_3 cracking.

Active Metal	Support Promoter	H_2 production rate mmol g_{cat}^{-1} min^{-1}	GHSV/WHSV mLg_{cat}^{-1} h^{-1}	Refs.
Ru 4.4 wt.%	$Ba(NH_2)_2$	8.1 (400 °C)	60,000	[15]
K-CoNi	$MgO-CeO_2-SrO$	8.26 (450 °C)	18,000	This Work
Ru 3.0 wt.%	$La-ZrO_2$	27.3 (450 °C)	30,000	[16]
K-CoNi	$MgO-CeO_2-SrO$	33.48 (500 °C)	30,000	This Work
Ru 3.5 wt.%	MgO DP	36.6 (500 °C)	36,000	[17]
K-CoNi	$MgO-CeO_2-SrO$	35.36 (525 °C)	32,000	This Work
Nano Ru **89 wt.%**	SiO_2	22.9 (450 °C)	30,000	[18]
K-CoNi	$MgO-CeO_2-SrO$	26.6 (475 °C)	30,000	This Work
Ru **5.0 wt.%**	K/CMK-3	24.2 (550 °C)	30,000	[19]
K-CoNi	$MgO-CeO_2-SrO$	47.51 (500 °C)	48,000	This Work

K-Ru	K-ZrO_2-KOH	25.7 (350 °C)	150,000	[20]
K-CoNi	MgO-CeO_2-SrO	57.72 (500 °C)	72,000	This Work

Notes: *H_2 production rates here are calculated based on total weight of catalyst. If calculated based on catalyst volume, our Ru-free catalyst would outperform other Ru catalysts.*

Table S4. A summary of non-precious monometallic catalyst for NH_3 cracking.

Active Metal	Support Promoter	Conversion At 450 °C	GHSV	Temp for 99 % conversion	Ref.
NiMoN	Al_2O_3	~10	3600 h^{-1}		[21]
HEA-Co25Mo45	-	< 59 %	36000 mL h^{-1} g_{cat}^{-1}	>500 °C	[22]
Co	Mg mixed oxide Al,Ce,La	< 30 %	6000 h^{-1}	80% at 550 °C	[23]
Co	MgO-La_2O_3	30 %	6000 h^{-1}	90% at 550 °C	[24]
Ni	MgAl	20 %	6000 h^{-1}	>600 °C	[25]
CuZn	Al_2O_3	62 %	6000 h^{-1}	>600 °C	[26]
CoNi	α-Al_2O_3	15 %	6000 h^{-1}	>600 °C	[27]
Ni	CaNH	90 % 55%	15000 mL h^{-1} g_{cat}^{-1} 15000 mL h^{-1} g_{cat}^{-1}	500 °C 475 °C	[28]
K-CoNi	MgO-CeO_2-SrO	97.75 % 87.50 %	3600 h^{-1} 6000 h^{-1}	99% at 475 °C	This Work
K-CoNi	MgO-CeO_2-SrO	48 %	24,000 h^{-1}	99% at 500 °C	This work

CoNi	$Ce_{0.6}Zr_{0.3}Y_{0.1}O_2$	50%	6000 mL h^{-1} g_{cat}^{-1}	99% at 600 °C	[29]
K-CoNi	MgO-CeO_2-SrO	89.5 %	6000 mL h^{-1} g_{cat}^{-1}	99% at 475 °C	This work
K-CoNi	MgO-CeO_2-SrO	64%	18000 mL h^{-1} g_{cat}^{-1}	93%at 475 °C 99.99% at 500 °C	This work

Table S5. Comparison of the ammonia cracking performance in different membrane reactors (with the specific range of operation parameters).

Membrane	Performance		Parameters		NH_3 conversion, %	H_2 recovery, %	Refs.
	Selectivity H_2/N_2	Permeance $mol/m^2.s.Pa$	GHSV (ml/g.h)	T(°C), and P(bar)			
MFI zeolite membrane	11	0.55×10^{-7}	1,200	450°C, 7.0bar	94.6	77.5	[30]
CMS	75	3.5×10^{-7}	5,000	450°C, 7.0bar	98.9	93.7	
Pd/Ag on ceramic substrate	>10,000	12×10^{-7}	5,000	450°C, 7.0bar	99.1	90.6	
6.2 μm Pd/Ag membrane on Cs modified Ru/YSZ substrate	infinity	6.46×10^{-7}	3,000*	450°C, 5.0bar	95	84	[31]
Composite zeolite membrane	**>120**	**0.5×10^{-7}**	**33,000**	**500°C, 5.0bar**	**>99**	**87.5**	**This work**

* GHSV – NH_3 feed flowrate divided by the volume of the YSZ supported Ru catalyst.

Table S6. Comparison of the ammonia cracking performance in a fixed bed (with the specific range of operation parameters)

Catalysts	Parameters		NH_3 conversion	Refs.
	WHSV (mL/g. h)	T(°C) /P(bar)		
3 % Ru/1 % Y/ 12 % K/Al_2O_3	1,200	450 °C, 7.0 bar	92.8	[30]
0.41 wt% Ru/ YSZ catalyst	3,000*	450 °C, 5.0 bar	50	[31]
Ru/Al_2O_3	2,400	450 °C, 5.0 bar	98.2	[32]
CoNi-oxides	**10,000**	**450°C,** **1.5 bar**	**97.7**	**This work**

* GHSV – NH_3 feed flow rate divided by the volume of the YSZ supported Ru catalyst

Table S7. Comparisons of surface area, pore-volume, and CO_2-TPD peak area of $CoNi_{alloy}$ on different supports.

$CoNi_{alloy}$ on different support	**BET surface area (m^2g^{-1})**	**CO uptake (µmol/g) [a]**	**Crystallite size (nm)**	**NH_3 conversion 450 °C 10,000 h^{-1}**	**CO_2 TPD peak area**
MgO	12.04	32.8	20.25	41.0	0.015
CeO_2	10.43	78.1	16.65	72.5	0.010
SrO	19.25-	1.4	13.72	63.9	0.006
MgO-CeO_2	15.37	52.5	12.27	77.7	0.027
MgO-CeO_2-SrO	34.14	109.2	11.65	83.3	0.037
K-MgO-CeO_2-SrO	30.16	64.8	8.74	96.7	0.051

[a] CO uptake was calculated from the CO pulse chemisorption at 35 °C.

Table S8. Apparent activation energies and turnover frequencies at 450, 475, 500 °C of the $CoNi_{alloy}$ catalysts supported on different supports.

$CoNi_{alloy}$ on different support	**Apparent activation energy (kJ mol^{-1})**	**TOF (s^{-1}) 450 °C**	**TOF (s^{-1}) 475 °C**	**TOF (s^{-1}) 500 °C**
MgO	84.0	3.73	6.91	8.15
CeO_2	89.5	1.85	3.42	4.38
SrO	113.4	1.18	2.87	3.91
$MgO\text{-}CeO_2$	52.3	3.18	5.31	6.65
$MgO\text{-}CeO_2\text{-}SrO$	63.8	4.90	5.72	8.47
$K\text{-}MgO\text{-}CeO_2\text{-}SrO$	56.8	6.78	7.94	11.14

Table S9. Structural parameters of adsorbed NH_x and H species on pure Co, Ni, CoNi alloys and CeO_2 supported on the Co_2Ni alloy surface where $d_{M\text{-}N}$ is the bond distance between the metal surface and N, $d_{N\text{-}H}$ is the bond distance between the N and H, h is the height of the adsorbate above the surface plane, and ∠HNH is the bond angle between the two N-H bonds.

		Co (111)	**Co_2Ni**	**$CoNi_2$**	**Ni (111)**	**Ceria/ Co_2Ni**
NH_3	**$d_{M\text{-}N}$ (Å)**	2.10	2.08	2.09	2.02	2.09
	$d_{N\text{-}H}$ (Å)	1.02	1.02	1.02	1.02	1.02
	h (Å)	2.10	2.08	2.09	2.02	2.09
	∠HNH (°)	108.60	108.70	108.60	108.90	108.90
NH_2	**$d_{Co\text{-}N}$ (Å)**	1.98	1.96	1.95	-	1.93
	$d_{Ni\text{-}N}$ (Å)	-	-	1.94	1.93	2.01
	$d_{N\text{-}H}$ (Å)	1.02	1.02	1.02	1.02	1.02
	h (Å)	1.53	1.51	1.50	1.48	1.53
	∠HNH (°)	106.79	107.60	107.60	107.90	108.20
NH	**$d_{Co\text{-}N}$ (Å)**	1.86	1.85	1.83	-	1.83
	$d_{Ni\text{-}N}$ (Å)	-	1.86	1.85	1.83	1.91
	$d_{N\text{-}H}$ (Å)	1.03	1.02	1.02	1.02	1.02
	h (Å)	1.11	1.31	1.33	1.08	1.23
N	**$d_{Co\text{-}N}$ (Å)**	1.76	1.74	1.72	-	1.73
	$d_{Ni\text{-}N}$ (Å)	-	1.79	1.78	1.76	1.84
	h (Å)	0.93	1.22	1.21	0.98	1.04
H	**$d_{Co\text{-}H}$ (Å)**	1.75	1.75	1.76	-	-
	$d_{Ni\text{-}H}$ (Å)	-	1.70	1.70	1.70	1.73

	h (Å)	0.99	1.21	1.19	0.90	1.19

Table S10. Activation barrier (E_a) and reaction energy (E_r) of the elementary steps of ammonia decomposition and N_2 formation energy on the (111) surface of Co, Co_2Ni, $CoNi_2$, Ni, and CeO_2/ Co_2Ni in eV.

		Co*	**Co_2Ni**	**$CoNi_2$**	**Ni***	**CeO_2/ Co_2Ni**
$NH_3^* \rightarrow NH_2^* + H^*$	E_r	0.05	-0.05	0.04	0.13	0.07
	E_a	1.18	1.14	1.16	1.30	1.41
$NH_2^* \rightarrow NH^* + H^*$	E_r	-0.34	-0.33	-0.12	-0.26	-0.10
	E_a	0.67	0.37	0.81	0.74	0.44
$NH^* \rightarrow N^* + H^*$	E_r	0.17	0.28	0.33	0.37	0.28
	E_a	1.22	1.23	1.30	1.41	1.31
$2 N^* \rightarrow N_2$ (gas)	E_r	0.64 (0.62*)	0.61	0.19	0.01 (0.49*)	0.22
	E_a	1.87 (1.86*)	1.52	1.62	1.73 (1.86*)	0.82

* Values from reference 8

REFERENCES:

[1] H. Zhang, Y. A. Alhamed, A. Al-Zahrani, M. Daous, H. Inokawa, Y. Kojima, L. A. Petrov, *International Journal of Hydrogen Energy* **2014**, *39*, 17573-17582.

[2] E. A. Kyriakidou, J. Lee, J.-S. Choi, M. Lance, T. J. Toops, *Catalysis Today* **2020**, https://doi.org/10.1016/j.cattod.2020.1005.1019.

[3] Y. Du, C. Jiang, W. Xia, L. Song, P. Li, B. Gao, C. Wu, L. Sheng, J. Ye, T. Wang, J. He, *Journal of Materials Chemistry A* **2020**, *8*, 55-61.

[4] J. Chen, P. Rohani, S. G. Karakalos, M. J. Lance, T. J. Toops, M. T. Swihart, E. A. Kyriakidou, *Chemical Communications* **2020**, *56*, 9882-9885.

[5] G. Kresse, J. Furthmüller, *Physical Review B* **1996**, *54*, 11169-11186.

[6] G. Kresse, D. Joubert, *Physical Review B* **1999**, *59*, 1758-1775.

[7] J. P. Perdew, K. Burke, M. Ernzerhof, *Physical Review Letters* **1996**, *77*, 3865-3868.

[8] P. E. Blöchl, *Physical Review B* **1994**, *50*, 17953-17979.

[9] D. F. Shanno, *Mathematics of Computation* **1970**, *24*, 647-656.

[10] G. Henkelman, H. Jónsson, *The Journal of Chemical Physics* **1999**, *111*, 7010-7022.

[11] X. Duan, J. Ji, G. Qian, C. Fan, Y. Zhu, X. Zhou, D. Chen, W. Yuan, *Journal of Molecular Catalysis A: Chemical* **2012**, *357*, 81-86.

[12] X. Duan, X. Zhou, D. Chen, in *Catalysis, Vol. 25*, The Royal Society of Chemistry, **2013**, pp. 118-140.

[13] A. M. Karim, V. Prasad, G. Mpourmpakis, W. W. Lonergan, A. I. Frenkel, J. G. Chen, D. G. Vlachos, *Journal of the American Chemical Society* **2009**, *131*, 12230-12239.

[14] F. R. García-García, A. Guerrero-Ruiz, I. Rodríguez-Ramos, *Topics in Catalysis* **2009**, *52*, 758-764.

[15] Z. Wang, Y. Qu, X. Shen, Z. Cai, *International Journal of Hydrogen Energy* **2019**, *44*, 7300-7307.

[16] B. Lorenzut, T. Montini, C. C. Pavel, M. Comotti, F. Vizza, C. Bianchini, P. Fornasiero, *ChemCatChem* **2010**, *2*, 1096-1106.

[17] X. Ju, L. Liu, P. Yu, J. Guo, X. Zhang, T. He, G. Wu, P. Chen, *Applied Catalysis B: Environmental* **2017**, *211*, 167-175.

[18] L. Yao, T. Shi, Y. Li, J. Zhao, W. Ji, C.-T. Au, *Catalysis Today* **2011**, *164*, 112-118.

[19] L. Li, Z. H. Zhu, G. Q. Lu, Z. F. Yan, S. Z. Qiao, *Carbon* **2007**, *45*, 11-20.

[20] S.-F. Yin, B.-Q. Xu, S. Wang, C.-t. Au, *Applied Catalysis A-general* **2006**, *301*, 202-210.

[21] C. Liang, W. Li, Z. Wei, Q. Xin, C. Li, *Industrial & Engineering Chemistry Research* **2000**, *39*, 3694-3697.

[22] P. Xie, Y. Yao, Z. Huang, Z. Liu, J. Zhang, T. Li, G. Wang, R. Shahbazian-Yassar, L. Hu, C. Wang, *Nature Communications* **2019**, *10*, 4011.

[23] S. Podila, Y. A. Alhamed, A. A. AlZahrani, L. A. Petrov, *International Journal of Hydrogen Energy* **2015**, *40*, 15411-15422.

[24] S. Podila, H. Driss, S. F. Zaman, A. M. Ali, A. A. Al-Zahrani, M. A. Daous, L. A. Petrov, *International Journal of Hydrogen Energy* **2017**, *42*, 24213-24221.

[25] K. Sato, N. Abe, T. Kawagoe, S.-i. Miyahara, K. Honda, K. Nagaoka, *International Journal of Hydrogen Energy* **2017**, *42*, 6610-6617.

[26] V. D. B. C. Dasireddy, B. Likozar, *Fuel* **2017**, *196*, 325-335.

[27] N. Shimoda, R. Yoshimura, T. Nukui, S. Satokawa, *JOURNAL OF CHEMICAL ENGINEERING OF JAPAN* **2019**, *52*, 413-422.

[28] K. Ogasawara, T. Nakao, K. Kishida, T.-N. Ye, Y. Lu, H. Abe, Y. Niwa, M. Sasase, M. Kitano, H. Hosono, *ACS Catalysis* **2021**, *11*, 11005-11015.

[29] C. Huang, H. Li, J. Yang, C. Wang, F. Hu, X. Wang, Z.-H. Lu, G. Feng, R. Zhang, *Applied Surface Science* **2019**, *478*, 708-716.

[30] J. Jiang, Q. Dong, K. McCullough, J. Lauterbach, S. Li, M. Yu, *Journal of Membrane Science* **2021**, *629*, 119281.

[31] Z. Zhang, S. Liguori, T. F. Fuerst, J. D. Way, C. A. Wolden, *ACS Sustainable Chemistry & Engineering* **2019**, *7*, 5975-5985.

[32] A. Di Carlo, L. Vecchione, Z. Del Prete, *International Journal of Hydrogen Energy* **2014**, *39*, 808-814.